Precambrian Research 378 (2022) 106760

Contents lists available at ScienceDirect

Precambrian Research

journal homepage: www.elsevier.com/locate/precamres

Mo isotope composition of the 0.85 Ga ocean from coupled carbonate and shale archives: Some implications for pre-Cryogenian oxygenation

E.M. O'Sullivan [a,*], T.F. Nägler [a], E.C. Turner [b], B.S. Kamber [b,c], M.G. Babechuk [b,d], S.P. O'Hare [b]

[a] Institute of Geological Sciences, University of Bern, Bern, Switzerland
[b] Harquail School of Earth Sciences, Laurentian University, Sudbury, Canada
[c] School of Earth & Atmospheric Sciences, Queensland University of Technology, Brisbane, Australia
[d] Department of Earth Sciences, Memorial University of Newfoundland, St. John's, Canada

ARTICLE INFO

Keywords:
Molybdenum isotopes
Palaeoredox
Neoproterozoic
Microbial carbonate
Black shale
Ocean oxygenation

ABSTRACT

This study addresses marine palaeoredox conditions of the mid-Neoproterozoic by analysing the Mo isotope, trace element, and U-Th-Pb isotope compositions of shallow water microbial carbonate, deep water pelagic carbonate, and shale from the Stone Knife Formation (SKF) in NW Canada. The U-Th-Pb isotope SKF systematics of reef microbialite carbonates, and the moderately expressed negative Ce anomalies are consistent with the presence of dissolved O_2 in the surface waters. Thirteen of 14 analysed samples yield a depositional $^{206}Pb/^{238}U$ regression age of 0.850 ± 0.028 Ga. The Mo isotope data ($\delta^{98}Mo$) are distinct for the microbial and pelagic carbonates and the deeper water shales, with the isotopically heaviest black shales 0.4 ‰ lighter than the heaviest carbonate. The bulk digestion carbonate $\delta^{98}Mo$ data scatter widely, ranging up to 1.64 ‰, and are not reproducible between repeat digestions. The spread in shallow-water carbonate $\delta^{98}Mo$ cannot be attributed to a single origin (e.g., admixture of silicate-hosted Mo) and probably reflects a combination of factors, including the complex pathway of Mo into microbial carbonates. Regardless, we propose a minimum $\delta^{98}Mo$ of 1.64 ‰ for the 0.85 Ga ocean, similar to other Neo- and Mesoproterozoic estimates from studies of proxies other than black shale. Our new black shale $\delta^{98}Mo$ data agree with most previous results from 1.8 to 0.7 Ga shales. If interpreted as reflecting seawater, this would mean a minimum oceanic $\delta^{98}Mo$ composition of only 1.29 ‰, implying a limited oxic reservoir compared to the modern Mo budget in agreement with previous studies. This study's results suggest that the discrepancy could also be explained by a systematic offset between $\delta^{98}Mo$ compositions of black shales and the overlying water columns, regardless of depositional environment, akin to the relative depth distribution of $\delta^{98}Mo$ in modern euxinic water columns such as the Black Sea. If valid, an implied heavier seawater $\delta^{98}Mo$ throughout the Proterozoic would indicate that the magnitude of the Mo oxic sink remained relatively stable throughout the Proterozoic, shifting the apparent expansion of oxygen towards the younger boundary of the interpreted onset of the NOE (ca. 1.0–0.54 Ga).

1. Introduction

The Great Oxidation Event (GOE; 2.50–2.22 Ga; Holland, 2006; Warke et al., 2020; Poulton et al., 2021) has captured the attention of the geochemical community as the first significant, global increase in free oxygen in Earth's atmosphere from < 0.001 % pre-GOE (Farquhar et al., 2000; Holland, 2006) to between 0.1 and 5 % present atmospheric level (PAL) between 2.5 and 0.8 Ga (Canfield et al., 2018; Johnson et al., 2014; Liu et al., 2021; Planavsky et al., 2014, 2016, 2020; Rye and Holland, 1998; Zhang et al., 2016). The later rise in oxygen during the Neoproterozoic, termed the Neoproterozoic Oxygenation Event (NOE, ca. 1.0 to 0.54 Ga; Och and Shields-Zhou, 2012), has emerged as the more substantial step towards oxygenation of Earth's atmosphere, with possible profound implications for the advent of complex animal life (e.g., Mills and Canfield, 2014). The NOE occurred against the backdrop of some of the most dramatic climatic and tectonic events in Earth's history, including the assembly and dispersal of supercontinent Rodinia and the subsequent assembly of Gondwanaland (Li et al., 2008; Mezger and Cosca, 1999; Veevers, 2004), and associated intermittent (near-) global glaciations (Hoffman and Li, 2009; Pu et al., 2016; Rooney et al., 2015). Finally, newly emerging evidence points towards a third increase in oxygen termed the Palaeozoic Oxygenation Event, resulting in oxygen

* Corresponding author at: GEOMAR Helmholtz Centre for Ocean Research, Kiel, Germany.
E-mail address: edel.osullivan@geo.unibe.ch (E.M. O'Sullivan).

https://doi.org/10.1016/j.precamres.2022.106760
Received 14 February 2022; Received in revised form 23 April 2022; Accepted 29 May 2022
Available online 14 June 2022

levels reaching those similar to the modern day (Krause et al., 2018; Tostevin and Mills, 2020).

Early reconstructions of Proterozoic oxygenation primarily envisioned a stepwise, unidirectional increase in oxygen from the GOE through to the Ediacaran period, featuring steady, low oxygen levels and including a long period of geochemical stasis during the Meso- and early Neoproterozoic (Lyons et al., 2014; Och and Shields-Zhou, 2012; Reinhard et al., 2013; Scott et al., 2008). In the marine realm were parallel shifts in redox conditions, where prevailing anoxic, Fe(II)-rich (ferruginous) oceans before 1.8 Ga gave way to widespread stratified ferruginous conditions with a mildly oxygenated surface layer and euxinic basins developing in restricted areas of high organic input through the Mesoproterozoic (Brocks et al., 2005; Canfield, 1998; Canfield et al., 2008; Gilleaudeau et al., 2020; Planavsky et al., 2011; Poulton et al., 2004, 2010; Poulton and Canfield, 2011; Reinhard et al., 2013). More recent geochemical investigations have argued for a significantly more dynamic, spatially heterogeneous, "pulsed" oxygenation occurring against a background of slowly increasing, albeit low baseline levels of O_2 (e.g., Chen et al., 2020; Luo et al., 2021; Lyons et al., 2021; Mukherjee et al., 2018; Sperling et al., 2014; Wei et al., 2021; Zhang et al., 2018) that may not have reached modern levels until well into the Palaeozoic (Krause et al., 2018; Tostevin and Mills, 2020). Despite the surge in available geochemical data, comprehensive palaeoredox reconstructions of the Precambrian oceans are constantly changing, often contradictory and are challenging to reconcile, obstructing the ultimate endeavour to assemble a single account of the evolution of the Earth's surface environment and, accordingly, the evolution of life.

A significant challenge in reconciling the available geochemical data is the vast array of proxies used from diverse archives and environments, each with unique complexities associated with preservation and diagenesis, different spatiotemporal constraints and resolutions, and biases related to depositional environment. One example is molybdenum (Mo) isotopes as a palaeoredox proxy. Since the pioneering work, Mo isotopes in marine sedimentary rocks have gained a reputation as a robust palaeoredox proxy (Arnold et al., 2004; Baldwin et al., 2013; Barling et al., 2001; Cheng et al., 2018; Czaja et al., 2012; Eroglu et al., 2015; Gilleaudeau et al., 2020; Kendall et al., 2011, 2015; Kurzweil et al., 2015a, 2015b; Luo et al., 2021; Ostrander et al., 2020; Siebert et al., 2003; Thoby et al., 2019; Voegelin et al., 2010; Wen et al., 2011; Wille et al., 2007, 2008; Xu et al., 2012), owing to the well-characterized redox-driven isotope fractionation of Mo in the Earth-surface environment. Molybdenum enters the surface environment via the oxic weathering of continental sulfides, Ti-bearing minerals, and sedimentary rocks such as shale and sulfate evaporite (Greaney et al., 2018; Miller et al., 2011). Together the sources yield an average continental crustal reservoir with an estimated δ^{98}Mo signature of between 0.0 and +0.4 ‰ (Arnórsson and Óskarsson, 2007; Greber et al., 2014, 2015; Liu et al., 2020; Siebert et al., 2003; Voegelin et al., 2014; Willbold and Elliott, 2017; Willbold et al., 2016; Zhao et al., 2016; relative to NIST SRM 3134, in which δ^{98}Mo is defined as 0.25 ‰ following Nägler et al. (2014)). Released Mo is transported via rivers as the highly mobile, conservative molybdate oxyanion (MoO_4^{2-}) to the ocean, where it has a residence time of 450 to 800 k.y. (Collier, 1985; Erickson and Helz, 2000; Lutfi Firdaus et al., 2008; Miller et al., 2011), leading to its homogeneous distribution at a concentration of 0.11 μM (Collier, 1985).

Dissolved Mo in ocean water is isotopically far heavier than its primary bedrock source, with a homogeneous δ^{98}Mo of +2.3 ‰ (Nakagawa et al., 2012). This offset starts to be generated in terrestrial environments as Mo is cycled from land to sea (e.g., Archer and Vance, 2008), but is mainly caused by the co-precipitation and burial of MoO_4^{2-} ions with (Fe)Mn-oxyhydroxides formed in the oxic ocean, a process shown to favour incorporation of light isotopes (Barling and Anbar, 2004; Goldberg et al., 1996, 1998, 2009; Kashiwabara et al., 2011; Siebert et al., 2003). In the presence of sufficient levels of dissolved H_2S_{aq} in euxinic environments (>11 μM; Erickson and Helz, 2000; Helz et al., 2011), MoO_4^{2-} is converted to the highly particle-reactive tetrathiomolybdate ion (MoS_4^{2-}), which, assuming a constant pH and without substantial deep-water renewal (Algeo and Lyons, 2006; Arnold et al., 2004), is efficiently fixed to the sediment with limited net fractionation. Modern euxinic black shales have been found to closely reflect the coeval ocean water δ^{98}Mo composition (e.g., Nägler et al., 2005, 2011). Accordingly, the evolution of Proterozoic marine palaeoredox conditions has been traced via δ^{98}Mo values extracted from euxinic black shales during the GOE and in the run-up to the NOE, and during and after the Cambrian explosion (e.g., Cheng et al., 2018; Gilleaudeau et al., 2020; Kendall et al., 2009; Kurzweil et al., 2015a, 2015b; Ostrander et al., 2020; Wille et al., 2007, 2008; Xu et al., 2012).

However, uncertainties about the nature of Mo fixation to black shale in the absence of, or with variably sufficient levels of H_2S_{aq} has challenged this interpretation. Stepwise conversion of MoO_4^{2-} to MoS_4^{2-} through a series of intermediate thiomolybdates ($MoO_xS_{4-x}^{2-}$) is accompanied by a fractionation effect of −1.4 to −1.8 ‰ (Nägler et al., 2011; Romaniello et al., 2016). As a consequence, in the absence of robust evidence for truly euxinic conditions, the maximum δ^{98}Mo composition of black shales may only be taken as a minimum for that of ancient ocean water, which may have been isotopically heavier (e.g., Gilleaudeau et al., 2020).

The challenge posed by such uncertainties is demonstrated by the evolving compilation of literature δ^{98}Mo estimates of Proterozoic ocean water as more data emerges. Early studies revealed generally uniform maximum δ^{98}Mo values for sediments between 1.7 and 0.7 Ga, ranging from 1.1 to 1.2 ‰ (Arnold et al., 2004; Kendall et al., 2009; Dahl et al., 2011), and 1.4 ‰ at 1.8 Ga (Kendall et al., 2011) indicating a relatively stable oxic Mo sink in the interval immediately preceding the NOE, increasing only near the end of the Ediacaran towards values similar to those of modern seawater (see literature compilation in Kurzweil et al., 2015a). However, subsequent studies encompassing a wider range of archive types to include BIF, primary MnO_2 deposits and carbonate as well as further black shale archives have revealed an apparent fluctuating trend, extending a range of minimum ocean water δ^{98}Mo compositions up to 2.2 ‰ for the same time interval (Baldwin et al., 2013; Diamond et al., 2018; Goto et al., 2021; Luo et al., 2021; Ye et al., 2021). The prevailing interpretation now suggests the incidence of several transient "pulses" of expansion of the Mo oxic sink in a highly changeable Proterozoic redox setting, occasionally up to modern-like levels (Luo et al., 2021; Ye et al., 2021).

One way to resolve the inter-archive inconsistencies observed might be the application of a single proxy to two contemporaneous archives of different depositional origin in the same locality, thus generating two distinct geochemical perspectives of the same basin. This study combines δ^{98}Mo and trace element compositions extracted from ca. 0.890 Ga calcimicrobial reefs of the Stone Knife Formation (SKF), Little Dal Group (Mackenzie Mountains Supergroup, Northwest Territories, Canada), along with corresponding data from equivalent black shale of the same formation, in an attempt to further elucidate the discrepancy observed between different archives and refine the open ocean redox state at this time. Non-skeletal carbonates are fast becoming a staple proxy in the palaeoredox toolbox (Czaja et al., 2012; Eroglu et al., 2015; Luo et al., 2021; Thoby et al., 2019; Voegelin et al., 2009, 2010; Wen et al., 2011), with ongoing work seeking to refine this archive (Chen et al., 2021; Clarkson et al., 2020; Romaniello et al., 2016). Calcimicrobial reefs are ideally suited to this study: they grow within the photic zone removed from direct continental input, and elevated above the basin floor, which precludes the incorporation of significant amounts of detrital contamination. The two palaeoenvironmentally distinct, coeval shallow and deep water Mo isotope archives from the same basin offer an opportunity to explore the Mo cycle in a well-constrained setting, and will fill a temporal gap in the Proterozoic seawater Mo isotope evolution between 1.2 and 0.7 Ga. The stable isotope data are presented together with new U-Pb isotope data to constrain the timing of microbial carbonate deposition.

2. Geological background

Giant (~500 m thick, kms diameter; Turner et al., 1997, 2000a) calcimicrobial reefs of the mid-Neoproterozoic Little Dal Group, Mackenzie Mountains Supergroup (MMSG), Northwest Territories (Fig. 1), display framework compositions characteristic of both typical Proterozoic stromatolites and Phanerozoic calcifying microbes (Turner et al., 1993, 1997), and are thought to record an important transitional phase in the evolution of early reefs (Turner et al., 1993, 2000a,b). The Little Dal Group's depositional age is bracketed in-basin between 990 Ma (U-Pb detrital zircon; Rainbird et al., 2017) and 775 Ma (U-Pb igneous zircon; Milton et al., 2017). The depositional age of the SKF has not previously been dated directly. Chemostratigraphic and sequence-stratigraphic correlation (Greenman et al., 2020) with the spatially and temporally related Amundsen basin indicates SKF deposition around ~890 Ma (Re-Os black shale; van Acken et al., 2013).

The lower Little Dal Group consists of a succession of carbonate and terrigenous clastic strata (Aitken, 1981; Turner and Long, 2012) that accumulated on a slowly subsiding ramp in an epicratonic basin in the interior of supercontinent Rodinia (Aitken, 1981; Batten et al., 2004; Turner and Long, 2008), overlying fluviodeltaic to shallow-marine strata of the Katherine Group (Fig. 2; Aitken, 1981). The 30–45-m-thick basal Dodo Creek Formation consists of siltstone and sandstone deposited in a shelf environment and is overlain by 15 m of transgressive oncoid grainstone containing local columnar stromatolite bioherms (Turner et al., 1997; Turner and Long, 2012) that mark the transition to two coeval but laterally equivalent formations: the Silverberry Formation, deposited in a shallow-marine ramp environment (Batten et al., 2004), and laterally equivalent deeper-water deposits of the Stone Knife Formation (SKF), the focus of this study. The SKF consists of ~500 m of carbonate mudstone, siltstone, grey and minor black shale and stromatolitic carbonate reefs, and is overlain by shallow-marine to peritidal carbonate rocks of the Gayna Formation (Turner and Long, 2012).

Giant reefs of the SKF are interpreted to have accumulated below fairweather wave-base but within the photic zone in an epicratonic basin, over 150 km away from the corresponding shallow-marine ramp environment of the laterally equivalent Silverberry Formation (Fig. 2). The overlying SKF consists of four shale-to-carbonate transgressive–regressive cycles (members 1–4) and calcimicrobial pinnacle reefs that span the entire thickness of the formation. In carbonate strata of member 1, a non-calcimicrobial stromatolite biostrome developed regionally, including on reef flanks. Members 2–4 consist of 'background' shale and siltstone punctuated by episodes of pelagic lime precipitation in the water column (Greenman et al., 2020), which accumulated on the basin floor below the photic zone and predominantly below storm wave-base. Sedimentological evidence indicates that the Little Dal reefs exhibited considerable palaeotopographic relief, standing at least several tens of metres above the surrounding basin floor and maintaining their growth surfaces within the photic zone. Late sea-level highstands and lowstands related to regional precipitation of pelagic carbonate mud were also associated with reef expansion and shedding of reef debris onto reef flanks, whereas transgressions were associated with reef aggradation and deposition of shale or argillaceous carbonate sediment in off-reef areas (Turner et al., 1997; Greenman et al., 2020).

The Little Dal reefs are composed of the lithified remains of microbial communities in a carbonate matrix, built predominantly by a community of well- to poorly-preserved filamentous cyanobacteria and probably acted as comparatively well-oxygenated "oases" in an otherwise low-oxygen ocean (Turner, 2021). When well preserved, the micritic calcimicrobial filaments form a distinctive microstructure containing large volumes of marine calcite cement in the 10- to 50-μm-scale spaces between the 10-μm-scale calcified, micritic filaments (or their degraded equivalents). Microbial filaments are identified by their variably preserved, elongate micritic sheaths or less well-preserved micrite clots, which are encased in marine cement, with millimetric to centimetric framework voids lined with thicker rinds of isopachous, cloudy, fibrous marine calcite cement (Turner et al., 1993, 2000a,b), as well as late, clear, blocky burial cements. Carbonate precipitation occurred either during the lifespan of the cyanobacteria, or within days or weeks of death related to organic matter degradation (Turner et al., 2000a,b), and so calcification occurred within the living part of the mat. Given the scale of the calcimicrobes and their enclosing volumes of marine cement in the stromatolite microstructure, it must be assumed that any spot analysis in or picked microsample from microbialite includes both calcimicrobial micrite and its enclosing coeval marine cement. The calcimicrobial carbonates and deeper-water pelagic lime mudstones are here referred to as "reef" and "off-reef" carbonates, respectively. The specific localities and individual reefs sampled for this study are outlined in the following section.

Shale and shaly carbonate of the deep-water parts of the SKF were deposited during transgressions, and member 2 locally contains black

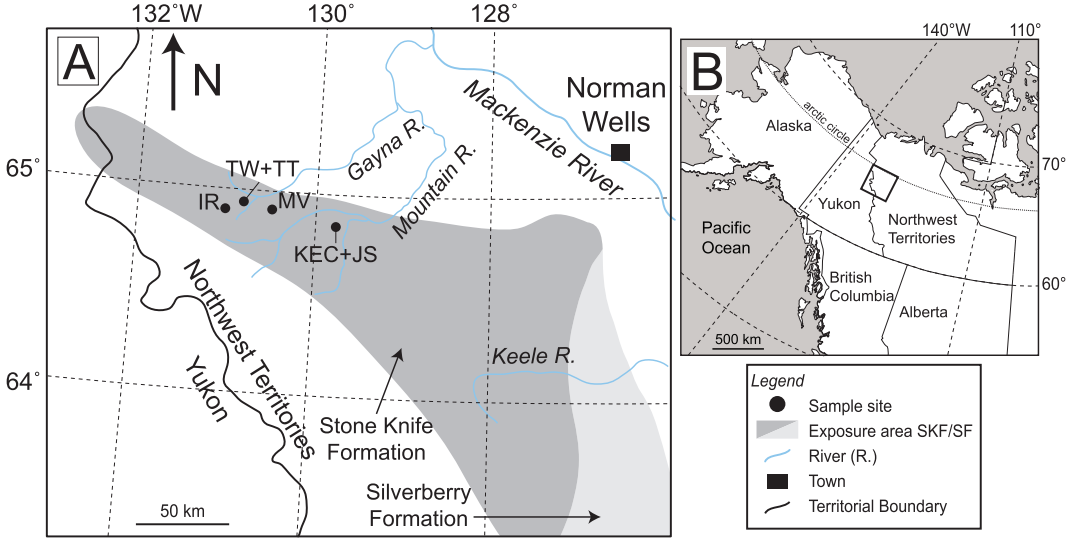

Fig. 1. A: Simplified map showing geographic location of the Stone Knife (SKF) and Silverberry (SF) Formations and sample sites within the SKF, modified after Turner et al. (1997). Light and dark grey shaded areas show exposure areas of the SKF and SF, respectively. Reef identification: MV = Queen Medb Reef; TW = Table Reef West; TT = Table Top Reef; KEC = Knife Edge Central Reef; IR = Intrepid Reef; JS = Reference section for the Stone Knife Formation. **B:** Simplified map of north-western Canada. Black box shows location of study area in A.

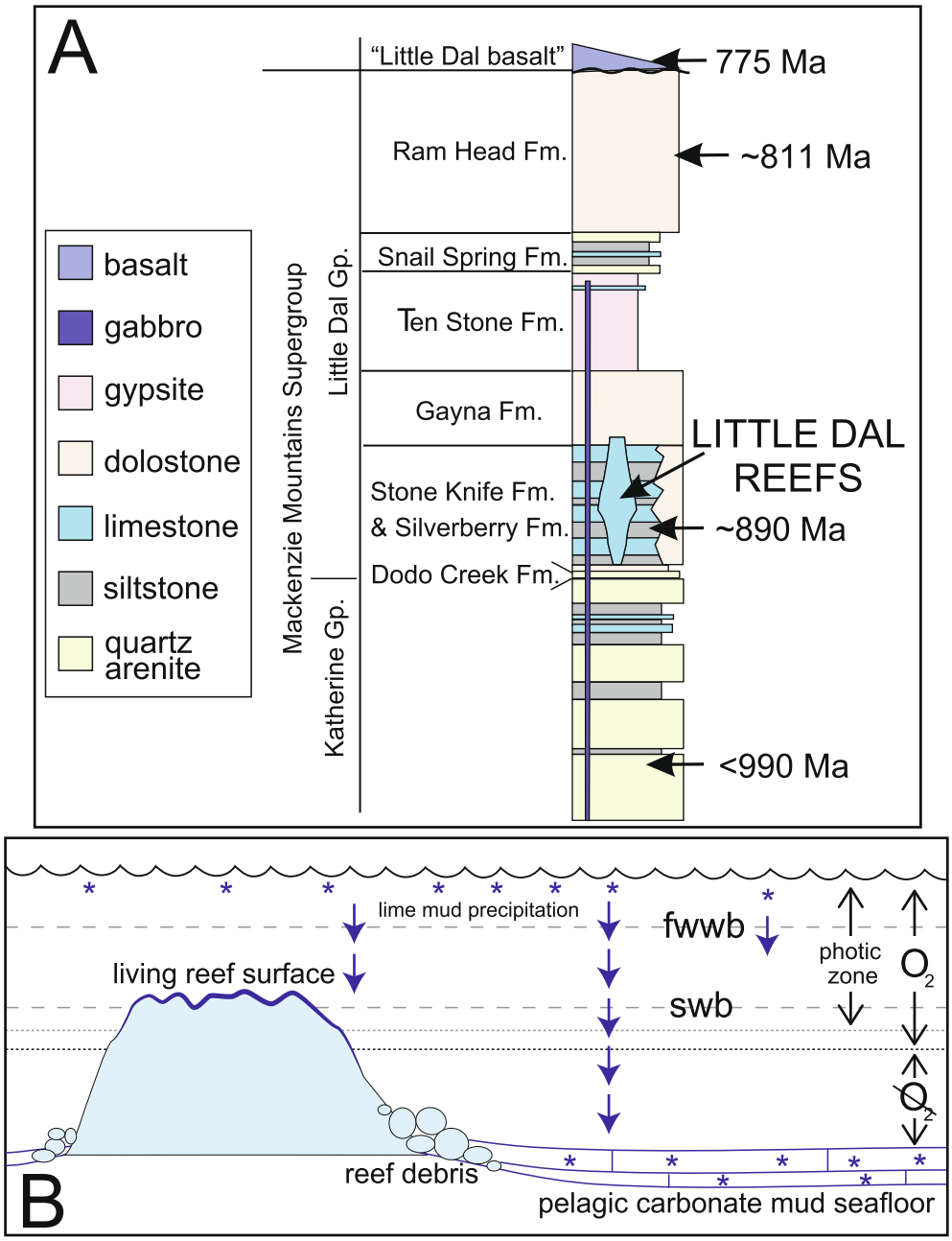

Fig. 2. A: Stratigraphy of the Little Dal Gp., after Turner and Long (2012) and Long and Turner (2012). The Little Dal reefs are part of the Stone Knife Formation. Maximum depositional age of the Mackenzie Mountains Supergroup <990 Ma (U-Pb detrital zircon; Rainbird et al., 2017); minimum depositional age >775 Ma (Pb-Pb igneous zircon; Milton et al., 2017). Stone Knife Formation depositional age is ~890 Ma, based on chemostratigraphic and sequence stratigraphic correlation with the Boot Inlet Fm. (van Acken et al., 2013; Greenman et al., 2020). The ~811 Ma Bitter Springs C isotope excursion is present in the Ram Head Fm. (Halverson, 2006). **B:** Configuration of reef and off-reef settings during late sea-level highstands of cycles 2 and 3. Reef progradation during late highstands and lowstands resulted in accumulation of reef-derived debris at reef bases. Carbonate mud precipitated in upper water column (asterisks) but accumulated on basin floor. fwwb = fair weather wave base. swb = storm wave base. Dynamics and water-column interfaces based on sedimentological criteria in Turner et al. (1997) and Greenman et al. (2020). Photosynthetic reef-builders may have created an 'oasis' of unusually high dissolved O_2 in the vicinity of reefs.

shale (Turner et al., 1997; Turner and Long, 2008, 2012; Greenman et al., 2020). The black shale analysed in this study was deposited in the deepest part of a subaqueous depocentre between two transfer faults in a zone of subtle crustal extension (Turner and Long, 2008). The Stone Knife Formation is unmetamorphosed and largely unaffected by deformation (Turner and Long, 2012).

3. Methods

The methodology described here focuses on the rationale behind sample selection and analytical strategy. Detailed sample and thin section descriptions are provided in Supplementary Information 1 and Supplementary Figure S2. All other methods, sample preparation and analytical techniques are described in Supplementary Information 2, including preparation for, and analysis of, Mo isotope analysis, trace and major elements, U/Pb isotopes, C + O isotopes and total organic content (TOC).

3.1. Sampling rationale

This study consists of two separate datasets pertaining to two different sampling and analytical campaigns carried out between 2009 and 2019, which are reconciled here to provide a full geochemical picture of the SKF depositional basin (see Supplementary Table S1 for overview of samples and analyses in both campaigns). Initial sampling and analyses during the first campaign were performed at Laurentian University as a pilot study of carbonate trace element geochemistry, and for U-Th-Pb systematics and U-Pb isotope dating of the calcimicrobial reefs. Targeted samples were from Intrepid Reef (IR), Knife Edge Central Reef (KEC), Table West Reef (TW) and Table Top Reef (TT), and the data from these samples are grouped as Sample Set A (distinguished as green symbols in figures). Sample thin sections from Sample Set A were first analysed *in situ* for YREE via LA-ICP-MS using both spot and line analysis. A selection of these samples were further analysed via solution ICP-MS for YREE as a comparison of bulk carbonate composition to the *in situ*

analysis of the corresponding samples, and to determine accurate U-Th-Pb ratios. These aliquots were subsequently purified for Pb isotope analysis.

The acquisition of an accurate U-Pb isotope age from samples of Sample Set A, as well as initial indications of water column chemistry revealed by YREE analysis identified the Little Dal reefs as suitable candidates for a Neoproterozoic seawater Mo isotope archive. The second campaign, however, targeted samples obtained primarily from Queen Medb Reef (MV), and Intrepid Reef (IR), which offered samples from almost all reef growth stages (see next section), resulting in a more comprehensive chemostratigraphy. All data pertaining to this campaign were obtained between 2017 and 2019, and are grouped as Sample Set B (distinguished as blue symbols in figures) – the main focus of this study. Off-reef, deeper-water carbonate and shale samples of section JS were also analysed during this campaign, and are included in Sample Set B. All samples in Sample Set B were analysed for stable Mo, C and O isotopes and C_{org} at the University of Bern, and major and trace elements via solution ICP-MS at Trinity College Dublin.

3.2. Sample collection and selection

Samples were collected over several field campaigns between 1992 and 2009 (Supplementary Table S1) prior to this study. The field area was glaciated until ~8 ka, and so exposures are generally minimally weathered. No single reef exposure provides access to all reef growth stages, and no single stratigraphic section covers the entire off-reef succession. Reef samples used in this study consist of fist-sized samples from a vertical outcrop transect through reef stages II and III in reef MV, several outcrop samples from stage IV of reef IR, and samples from a drill-core through stage V in reef IR. Additional reef samples from stage II and stage IV of reefs KEC and TT, respectively, were also included in this study. Deep water carbonate strata were sampled in stratigraphic section JS (reference section for the SKF; Greenman et al., 2020; Turner and Long, 2012). Reef stage I as well as off-reef member 3 were not sampled due to significant visible terrigenous input. Each shale sample was collected after excavating a shallow pit to minimise the influence of modern weathering, and organic-rich shale was removed by pocket-knife. Approximate stratigraphic positioning of samples selected for each geochemical study are depicted in Supplementary Figure S1. The SKF deep water and Little Dal reef sample stratigraphic positions are approximately linked through sequence stratigraphy and chemostratigraphic correlation using the SKF carbonate $\delta^{13}C$ curve (Supplementary Figure S1-A) both conducted by Greenman et al. (2020).

Detailed petrographic descriptions and thin section photographs of a representative selection of samples (MV448, MV489 and GRiii8) are provided in Supplementary Information 1 and Supplementary Figure S2, respectively. Sample MV448 contains a small (<1%) proportion of patchy secondary, euhedral dolomite crystals among the microbial carbonate fabric and is associated with pressure solution seams, as well as fracture-filling carbonate (0.5 mm wide) consisting entirely of dolomite. Sample staining with potassium ferricyanide and alizarin red S solution (Supplementary Figure S2-B) as described in Dickson (1965) exposes up to 15 % dolomite within the micritic matrix and marine cement; nonetheless the samples are dominantly composed of calcite. Additionally, throughout the samples are small (up to 20 μm) to tiny (<0.1 μm) opaque minerals, some of which remain dark under reflected light and are probably composed of dense micrite and organic matter. Qualitative inspection via Raman spectroscopy using a LabRam Raman Spectrometer with a red (785 nm) laser using a 100x objective lens and acquiring Raman spectra using the LabSpec 4.14 software indicate that a variety of oxides and sulfides are present. Spectra were identified through comparison of peak wavelengths with those in the RRUFF2 database and in the reef carbonates MV448 and MV489 include hematite, brookite, rutile, anatase, arsenopyrite and chalcocite (Supplementary Figure S3). These minerals are too small to correctly identify growth textures to establish the timing of growth. The off-reef carbonate sample (GRiii8) contains abundant euhedral hexagonal to pentagonal pyrite, with reddish coatings identified most closely as goethite. As a bulk-digestion technique was employed here, this study did not include an in-depth investigation into the mineral-textural characteristics of every sample prepared for Mo isotope or geochemical analysis, and it is possible that a far wider variety of oxides and sulfides are present in minute quantities in the samples.

Initial screening of samples from MV and IR reefs for excessive diagenesis including pervasive dolomitisation and/or the presence of significant detrital silicate material eliminated any samples that had overwhelmingly non-calcitic components, however the inclusion of minor secondary components as described above, which are present in trace amounts in almost all samples could not be eliminated from a bulk-rock geochemical study employed here.

4. Results

All data pertaining to this study are reported in Tables 1–4 and Supplementary Tables S1-4, both in the electronic appendix attached to this manuscript.

4.1. U-Pb isotope age constraints

Samples for Pb isotope analysis and U-Pb age dating were selected from Sample Set A based on initial $^{206,207,208}Pb$ signals recorded during the trace element run that suggested the presence of uranogenic Pb and a general absence of elevated ^{208}Pb. The analysed $^{206}Pb/^{204}Pb$ ranged from 18.4 to 22.6, while $^{208}Pb/^{204}Pb$ is near constant at 38.11 ± 0.18, reflecting the in-growth of radiogenic Pb from U decay in the absence of significant ^{232}Th decay. This is supported by the observed $^{232}Th/^{238}U$ much lower than the silicate Earth value of 4. Uranium and Pb concentrations in the selected carbonate samples ranged from 0.036 to 1.38 μg/g and 0.11–76.92 μg/g, respectively, while Th concentrations were as low as single digit ng/g.

Observed $^{238}U/^{204}Pb$ and $^{206}Pb/^{204}Pb$ ratios range from 1.04 ± 0.004 to 29.88 ± 0.12 and 18.40 ± 0.03 to 22.56 ± 0.04, respectively. There is a strong positive correlation between $^{238}U/^{204}Pb$ and $^{206}Pb/^{204}Pb$ ratios (MSWD to 3.8). Omitting one outlier sample from 14 datapoints yields an isochron with a MSWD of 1.06, i.e. all scatter around the regression can be readily explained by measurement uncertainties alone. The resulting age is 0.845 ± 0.028 Ga (Fig. 3). The slight offset of the single outlier probably reflects some open-system

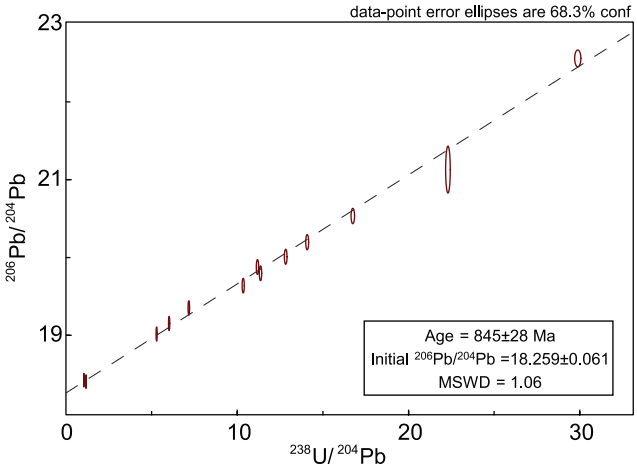

Fig. 3. U-Pb isochron of reef microbialites giving an isochron age of 0.845 ± 0.028 Ga with an MSWD of 1.06. Samples with disturbed isotope ratios resulting from open-system behaviour of carbonates are excluded. Samples used to calculate depositional age are from reef stages IV and V, from the uppermost Stone Knife Fm (Supplementary Table S1).

behaviour, secondary mineral growth or diagenesis.

4.2. Mo concentration and δ^{98}Mo

Molybdenum isotope composition and [Mo] for the reef, off-reef, and shale samples of Sample Set B as analysed via the double spike method (Siebert et al., 2001; here denoted *DSM*) are presented in Table 2, and [Mo] data as analysed via solution ICP-MS (denoted *solnICP*) are displayed in Table 3. Overall $[Mo]_{DSM}$ in both reef and off-reef carbonates is low, ranging from 4.88 to 33.6 ng/g, and 9.70 to 186.5 ng/g, respectively, within the range of previously reported Precambrian carbonate [Mo] data (Eroglu et al., 2015; Thoby et al., 2019; Voegelin et al., 2010). $[Mo]_{solnICP}$ is considerably different from that analysed by DSM, ranging from 5.17 to 76.5 ng/g in the reef carbonates, 40.5 to 320 ng/g in the off-reef carbonates, and 7.10 to 5.57 μg/g in the shale samples. δ^{98}Mo varies from 0.35 to 1.64 ‰ (n = 31) in the reef carbonates, and a similar range in δ^{98}Mo was found in off-reef carbonates of 0.42 to 1.60 ‰ (n = 7). No correlation is seen between $[Mo]_{DSM}$ or $[Mo]_{solnICP}$ and δ^{98}Mo in either the reef or the off-reef samples (Figs. 4 and 5). Apart from sample MV489, no repeated carbonate δ^{98}Mo or [Mo] analyses performed on the same powdered sample reproduced within error, and differences of up to 0.9 ‰ are found between δ^{98}Mo data of the repeated samples digests (Figs. 4 and 5).

Shale samples have $[Mo]_{DSM}$ in the range of 1.50 and 4.78 μg/g. Although these values are similar to some Precambrian black shales used in previous palaeoredox studies (generally <5 μg/g, e.g., Dahl et al., 2011; Ostrander et al., 2020), they are at the far lower range of what might be expected of Mo-enriched black shales based on previously reported Mo data of Proterozoic and Phanerozoic age, which typically range from 30 to 50 μg/g and to up to several 100's of μg/g, respectively (see compilation of literature data in Thoby et al., 2019). The shale sample Mo isotope compositions fall within a much narrower range than those of the carbonate samples, ranging between 0.76 and 1.29 ‰, with a single outlier at 0.29 ‰.

4.3. Major and trace elements

Major and trace element data are reported in wt% or μg/g and values are listed in Table 3. Aluminium and Ti in the reef carbonates range from 0.01 wt% to 0.72 wt%, and 0.005 wt% to 0.03 wt%, respectively. Both the average Mo/Al and Mo/Ti are far lower than those of the upper continental crust composite of Taylor and McLennan (1985) and there is no correlation between Al or Ti and $[Mo]_{solnICP}$. Iron concentration is variable but low in the reef carbonates (between 0.04 and 0.34 wt%), but is higher in the off-reef carbonates, up to a maximum of 1.62 wt%. Manganese remains approximately the same in both reef and off-reef carbonate samples, between 0.01 and 0.06 wt%.

Yttrium and rare earth element (YREE) data from Sample Set A analysed by *in situ* methods (denoted *insitu*) are shown in Table 4. The widely used marine REE anomalies and elemental ratios are also listed in Tables 3 and 4. Total YREE (∑YREE) is low in the reef carbonates, ranging from 1.40 to 42.1 μg/g, is slightly higher in the off-reef carbonates (15.2 to 64.9 μg/g) and higher still in the shale samples (116 to 394 μg/g). YREEs were normalised to MuQ (Mud from Queensland, denoted MN; Kamber et al., 2005) because it is a suitable upper crustal composite for sources with suspected high basalt sediment source. Carbonate samples display a range of MuQ-normalised patterns from flat to typical seawater-like patterns in both solution- and *in situ*- analysed samples, namely a positive La-anomaly (La/La*), negative Ce-anomaly (Ce/Ce*) and positive Y-anomaly (Y/Ho) (e.g., Webb and Kamber, 2011). However, in most samples the typical open seawater LREE-depletion indicated by Pr/Yb ≪1 is lacking, and in some cases (particularly in the *in situ* data of coarse crystalline, sparry late crack-filling carbonate) an apparent HREE depletion or MREE enrichment is present. This relatively flat pattern has been noted previously as a characteristic of Precambrian (Kamber and Webb, 2001) and particularly Neoproterozoic carbonates (e.g., Shuster et al., 2018) and has variably been explained as deposition in near coastal environments, proximity to localised fluvial influx, from distinctive REE pattern of continental runoff, or an artefact of the modern UCC normalisation when the local source rocks differed significantly in composition (Kamber et al., 2014; Kamber and Webb, 2001; Ling et al., 2013).

Almost all carbonate sample data display a positive La anomaly in both solution- and *in situ*- analysed data, with $La/La^*_{solnICP}$ ranging from unity to 1.73 and from 0.56 to 3.91 in the less precise La/La^*_{insitu} data. MuQ-normalised Ce anomalies were calculated via the method of Lawrence and Kamber (2006). It was found that $Ce/Ce^*_{solnICP}$ is within a narrow range for all samples (0.91 to 1.05), but the less precise Ce/Ce^*_{insitu} have a higher range from 0.44 to 2.09. Y/Ho ranges in reef carbonate samples from chondritic (approx. 28) to strongly

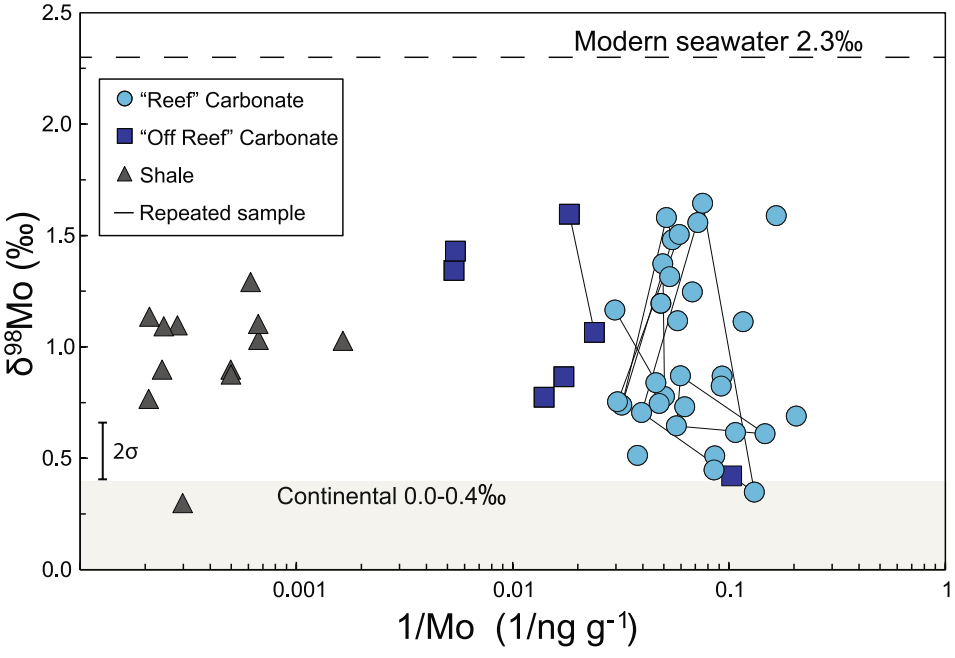

Fig. 4. Diagram of δ^{98}Mo vs inverse Mo concentration (1/Mo) of all SKF shale (n = 11) and carbonate (n = 28) samples analysed in this study, including repeated measurements (n = 12), in comparison to modern seawater δ^{98}Mo composition (dashed horizontal line, Nakagawa et al., 2012) and continental crust (grey-brown shaded area, see text for references). These diagrams are widely used to expose binary mixing and contamination. Solid lines connect repeated samples, as highlighted in Fig. 4. Individual measurement $2\sigma\bar{x}$ uncertainties are smaller than symbol size. 2σ standard deviation adopted from repeated measurements of limestone reference material BCS-CRM 393 of ± 0.13 ‰. [1/Mo] reported as calculated via DSM. Data plotted are from samples from Sample Set B and are listed in Table 2.

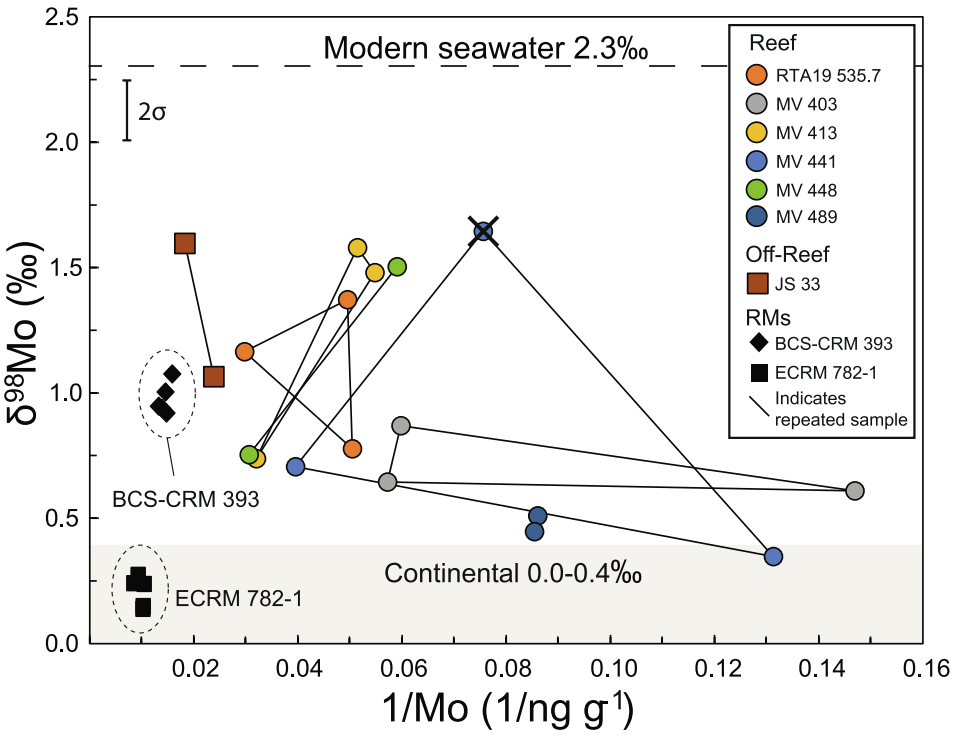

Fig. 5. Diagram of δ^{98}Mo vs inverse Mo concentration (1/Mo) of repeated measurements of selected carbonate samples of Sample Set B (n = 12, see methods for sample selection criteria) showing a lack of systematic mixing between identifiable Mo sources. Solid lines connect individual samples indicating 2 or 3 repeated measurements of separate dry powdered aliquots. Dashed horizontal line and grey-brown shaded area same as in Fig. 4. Individual measurement $2\sigma\bar{x}$ uncertainties are smaller than symbol sizes. 2σ standard deviation adopted from repeated measurements of limestone reference material BCS-CRM 393 of ± 0.13 ‰. Data plotted are listed in Table 2.

superchondritic (>44) with the majority of samples falling central in the range. Only seven solution-analysed carbonate samples display Y/Ho > 44, whereas Y/Ho of *in situ*-analysed samples range up to 75. Off-reef carbonate and shale sample Y/Ho ratios are close to chondritic (23.53 to 29.20).

4.4. C_{org}, C and O isotopes

Total organic carbon (TOC) of all carbonate (reef and off-reef) samples (Table 2) is between 0.07 and 0.38 wt%, with the exception of one anomalous off-reef lime mudstone sample with a TOC content of 2.42 wt%. Total organic carbon in shale samples similar to the range seen in previous black shale data (e.g., black shale compilation in Scott et al. (2008)), ranging from 2.17 to 8.24 wt%. Mo/TOC ratios in shale are varied but consistently low (between 0.33 and 0.82).

Results of both δ^{13}C and δ^{18}O (Table 2) are within the range previously reported for Precambrian carbonates (Fig. 8). δ^{13}C is consistently positive, between 3.41 and 6.52 ‰$_{VPDB}$, with one outlier of 0.57 ‰$_{VPDB}$, while δ^{18}O is consistently negative, with values between −2.57 and −14.05 ‰$_{VPDB}$. There is no obvious relationship between δ^{13}C and δ^{18}O (Fig. 8). Comparison of the 3 off-reef carbonate δ^{13}C and δ^{18}O results with those of the same samples as analysed by Greenman et al. (2020) shows close agreement (within max. 0.2 ‰ for δ^{13}C and 1.4 ‰ for δ^{18}O). Sample JS55 is from member 2, whereas samples JS95 and JS98 are from member 4, and these show an up-section increase in δ^{13}C. The reef samples show generally lighter δ^{18}O than that analysed in the corresponding SKF member by Greenman et al. (2020), whereas δ^{13}C is largely in agreement considering that the exact time-equivalent off-reef strata is not currently determined.

4.5. Trace metal enrichment in shales

Enrichment factors (EF) for redox-sensitive elements Mo, U, V and Cr (Table 2) were calculated for shale samples as $X_{EF} = [(X_{sample}/Al_{sample})/(X_{UCC}/Al_{UCC})]$, where X is the desired element (Algeo and Tribovillard, 2009) and UCC is an upper continental crustal composite representing the baseline concentration of these elements. An EF of >3 indicates significant enrichment of an element over the baseline, and >10 is extremely significant (Algeo and Tribovillard, 2009). Enrichment factors for ancient samples are sensitive to the UCC composite used, depending on the relative abundances of each element. Here, elements are normalised to both MuQ (Mud from Queensland; Kamber et al., 2005; Marx and Kamber, 2010) and to PAAS (Post Archaean Australian Shale; Taylor and McLennan, 1985), which have similar concentrations of Al (17.3 wt% vs 15.2 wt%, respectively) but differ in their Mo and Cr content by a factor of 3 (Mo content 0.48 μg/g vs 1.5 μg/g, respectively; Cr content 53.5 μg/g vs 110 μg/g, respectively). Uranium and V contents of MuQ and PAAS vary less significantly (U content 2.38 μg/g vs 2.8 μg/g, respectively; V content 69.5 μg/g vs 60 μg/g, respectively).

Enrichment factors calculated relative to PAAS for Mo, U and Cr are generally insignificant, while V is poorly to mildly enriched in the shales (Table 2). $Mo_{EF\text{-}PAAS}$ and $U_{EF\text{-}PAAS}$ range from 0.37 to 3.9 and 1.5 to 4, respectively. Enrichment factors calculated relative to MuQ are generally more significant, with $Mo_{EF\text{-}MuQ}$ and $U_{EF\text{-}MuQ}$ ranging from 1.3 to 14 and 1.9 to 7.3, respectively.

5. Discussion

Our approach to characterising the mid-Neoproterozoic ocean δ^{98}Mo composition was to construct a multifaceted geochemical framework of the SKF basin using Mo isotope and trace element data derived from different archives. This required several assumptions; first, that the instantaneous seawater geochemical and δ^{98}Mo composition was homogeneous across the SKF basin, especially in terms of the relatively long residence time of Mo in even mildly oxygenated conditions (Dahl et al., 2011; Kendall et al., 2011). Second, that all individual reefs housed broadly comparable microbial communities, physicochemical structure, porewater redox chemistries and gradients, and included a similar array of non-carbonate mineralogy. Third, that all individual reefs grew simultaneously within the SKF basin under the same (possibly temporally variable) environmental conditions, so that the geochemical fingerprints of each reef can be extrapolated and compared across the basin. Likewise, that all deeper water lime mudstones were deposited under similar redox conditions irrespective of sampling location. Third,

that the distribution of any natural, non-carbonate components within the sample frameworks would be effectively homogenised within each sample during preparation, and that inadvertent inclusion of these components would be identifiable through geochemical end member characterisation.

Considering the highly variable δ^{98}Mo and [Mo] compositions among both reef and off-reef carbonates, and the unsuccessful reproduction of δ^{98}Mo results among repeated digestions of the same carbonate samples (Fig. 5), one or more of the above assumptions was evidently not met. Since an identical preparation and analytical procedure was performed on each separate digestion obtained from the dry sample powders, and that powdered reference materials alongside each batch of carbonate samples including repeats reproduced within 0.12 ‰, inconsistent sample preparation or errors in analytical proceedings among repeats were here ruled out. The fact that the variability is observed within individual samples suggests that spatial differences in water column geochemistry is unlikely to control this variation as might be suggested by variability among different samples alone, or exerts only a small effect. As will be discussed in detail below, the variation likely points to the existence of several isotopically-distinct sources of Mo within each sample contributing to the bulk [Mo] and δ^{98}Mo composition that were not effectively homogenised during sample preparation.

This high level of variation in δ^{98}Mo was to some extent expected, at least among individual samples, as it has been observed in previous carbonate Mo isotope studies (e.g., Eroglu et al., 2015; Luo et al., 2021; Voegelin et al., 2009, 2010). However, since each analytical technique (MC-ICP-MS, solution ICP-MS, etc.) was performed on a separate dry sample aliquot, data produced from each cannot be directly compared, and any correlations between them, or lack thereof, may have been affected by differing extents of mixing of non-carbonate Mo and geochemical signatures. However, it is still reasonable to infer broad connections between each dataset based on their individual interpretations. Sample Set B consists of separate analyses of each sample for: i) Mo isotopes, ii) major and trace elements, iii) C and O isotopes, and iv) TOC, which cannot be compared directly. Repeated Mo isotope analyses are treated as separate data points in the following discussion but indicated by tie-lines in Figs. 4 and 5. Furthermore, as only one to two samples were analysed from each point in the stratigraphy of reefs MV and RT, a definitive chemostratigraphy for, and stratigraphic correlation between, the Little Dal reefs and SKF off-reef carbonates and shales was inferred to be impractical. Instead, the dataset will be treated as a whole, and the isotopically heaviest sample of the entire suite will be assumed to be the closest to coeval seawater. This approach has been employed in almost all previous Mo isotope studies of carbonates and shales (e.g., Gilleaudeau et al., 2020; Ostrander et al., 2020; Thoby et al., 2019; Voegelin et al., 2009, 2010). That being said, we retain the assumption that the overall seawater geochemical composition and redox stratification across the basin can be inferred from extrapolation of geochemical interpretations of individual reefs and sampling localities.

In contrast, δ^{98}Mo data of the shale samples do not show the same level of heterogeneity among samples, and it is assumed that any similar secondary effects that are typically expected in shale δ^{98}Mo data are not as pronounced as in the carbonate samples. As is discussed in detail below, this is most likely a result of the comparatively lower sensitivity of the δ^{98}Mo data to secondary components due to the overall higher Mo content of the shales relative to the carbonates. Additionally, the elevated Mo content of black shale is generally associated directly with sequestration of trace metals onto organic particles, linking each of these parameters. As such, the different datasets for the shale samples will be compared directly.

5.1. Depositional age of Little Dal reefs

The tightest correlative age constraint of the SKF places its deposition at 892 ± 13 Ma based on time-equivalent Boot Inlet Formation C isotope stratigraphy (Greenman et al., 2020; van Acken et al., 2013), clearly significantly pre-dating the Cryogenian Rapitan Group ('Sturtian glaciation') locally dated to 711 ± 0.24 Ma (Baldwin et al., 2016). The new ^{206}Pb/^{238}U regression age of 845 ± 28 Ma (Fig. 3) agrees with the range of ages implied by stratigraphic correlation, constraining the deposition of the SKF to this time. Both the Boot Inlet Formation date and the SKF date are from the upper parts of the respective time-equivalent formations; the reason for the slight discrepancy between the two dates remains unclear, but could possibly reflect a minor influence of slightly younger, petrographically imperceptible diagenetic phases in the SKF material.

5.2. Spatial geochemical heterogeneity of SKF microbial carbonates

Identification of the source of geochemical heterogeneity is crucial for extracting a robust carbonate δ^{98}Mo composition as a proxy for that of coeval seawater, and will first be explored here. Since Mo isotope fractionation upon incorporation into calcite is minimal (Chen et al., 2021), and calcification of the Little Dal reefs was geologically instantaneous within the microbial mat (Turner et al., 2000a,b), the pure carbonate end member can be considered as representative of the seawater δ^{98}Mo composition at the time of reef growth. Variability in microbial and skeletal carbonate δ^{98}Mo signatures and [Mo] similar to that observed in the Little Dal reef and off-reef samples has been attributed to the inclusion of secondary components of carbonates, namely silicate and other detrital material, and secondary minerals formed in porewaters related to complex small-scale elemental cycling in porewaters during early diagenesis (e.g., Chen et al., 2021; Eroglu et al., 2015; Luo et al., 2021; Romaniello et al., 2016; Voegelin et al., 2010). Selective dissolution of carbonate material (e.g., Clarkson et al., 2020) was not possible in the present study because of the very low Mo concentration in the complete-digested carbonate (as low as 5 ng/g, including all non-carbonate components). Instead, we attempted to differentiate among Mo sources through geochemical end-member identification. Both release of adsorbed Mo from the surfaces of secondary oxides, and leaching of Mo from detrital phases within the carbonate would be expected to result in a mixing behaviour between the two, or three isotopically distinct end-members. Both of these secondary components are typically characterised by isotopically light δ^{98}Mo relative to seawater (and thus the carbonate end member), and far higher [Mo] than pure carbonate. Conversely, no mixing trends are evident in the carbonate δ^{98}Mo data of this study in the δ^{98}Mo vs 1/[Mo] diagrams, in which simple HCl-leaching excluded full digestion of minor silicate phases (Figs. 4 and 5).

5.2.1. Evaluating the contributions from continental detritus

Molybdenum sourced from detrital silicates with an implied continental crust δ^{98}Mo composition of between 0.0 and 0.4 ‰ contributes to the overall Mo content of bulk carbonate (e.g., Clarkson et al., 2020; Eroglu et al., 2015), lowering the resulting bulk isotope value. Siebert et al., (2003) and Clarkson et al., (2020) determined that during bulk acid digestion, Mo is liberated from silicate phases to varying extents even during cold, weak HCl, HNO_3 or acetic acid leaching, resulting in a mixing effect between silicate and carbonate Mo sources in analyses of bulk carbonate. The release of metals from minor silicate into carbonate leachates, even when using weak acetic acid has also been demonstrated with unsupported thorogenic Pb isotope ratios (e.g., Kamber et al., 2004). Inspection of the carbonates did not expose obvious detrital material, though ultrafine-grained (<2 μm) detrital minerals may not have been detected. Minor Ti oxides brookite and anatase were identified in the Little Dal reef carbonates by Raman spectroscopy (Supplementary Figure S3) which likely derive from continental, rather than diagenetic sources. As Raman analysis was not exhaustive, it is possible that additional terrigenous material may have been overlooked.

Trace element data from full digests reveal many mixing relationships between seawater- and detrital-derived trace and REEs leading to

covariation between Y/Ho, Ti and the La anomaly (both highly sensitive to detrital contamination (Cabioch et al., 2006; Webb and Kamber, 2000), Fig. 6) as well as positive correlations between ∑REE and Al, Ti, Sc and Zr (not shown). Correction for detrital input is traditionally attempted using the $Mo_{solnICP}$/Ti ratios of commonly used continental compilations Post-Archaean Australian Shale (PAAS; Taylor and McLennan, 1985) or Upper Continental Crust (UCC; Rudnick et al., 2003). The Ti/Al ratio in all carbonate samples analysed is uniform (0.029 to 0.039, average 0.033) and is close to that of UCC (0.037; Rudnick et al., 2003), indicating a terrigenous source for both Ti and Al content, which is also petrographically evident by the presence of Ti oxides (Supplementary Figure S3). Elevated $Mo_{solnICP}$/Ti ratios above that of PAAS displayed by the majority of carbonate samples are here a distinguishable feature of authigenic Mo input, with higher $Mo_{solnICP}$/Ti associated with increasing Y/Ho where seawater geochemical signatures become dominant over detrital ones (Fig. 6). As a result, when applied to our data, such correction resulted in unrealistic estimates of detrital vs. authigenic Mo (denoted *auth*) and erroneously indicated an overwhelming continental Mo signature (between 4.5 and 853.9 % detrital Mo when corrected via Mo/Ti of UCC; Rudnick et al., 2003), which is precluded by the isotopically heavy signatures greater than typical continental crustal values, even where sample $Mo_{solnICP}$/Al is close to that of PAAS. The fully digested trace element data leave no doubt about the presence of a detrital phase harbouring at least some Mo, but the mixing relationships break down in the HCl-digests processed for Mo isotope analysis. This makes it impossible to mathematically correct the measured δ^{98}Mo for detrital influence.

5.2.2. *Evaluating the role of oxides and sulfides*

Clarkson et al. (2020) observed negative correlations between Mo content and δ^{98}Mo in bulk-digested pelagic-carbonate-rich sediment samples arising from the release of isotopically-light (up to 3 ‰ lighter than coeval seawater), exchangeable Mo derived from secondary diagenetic oxides. Romaniello et al. (2016) showed that a positive correlation between δ^{98}Mo and [Mo] in sediment core samples from the Bahamas was attributed to small-scale redox cycling of Mo within restricted carbonate sediment porewaters, where sulfate reduction dominates microbial processes and elevates porewater H_2S_{aq}. The variable adsorption and concentration of isotopically light Mo onto these phases has the strong potential to distort the bulk carbonate δ^{98}Mo signature. The Little Dal reef carbonates contain abundant, though overall minor (<1 %) oxides and sulfides throughout the microbial framework, ranging in size from 20 to ≪1 μm and including Fe and Ti oxides, and Cu and As sulfides (Supplementary Information 1,

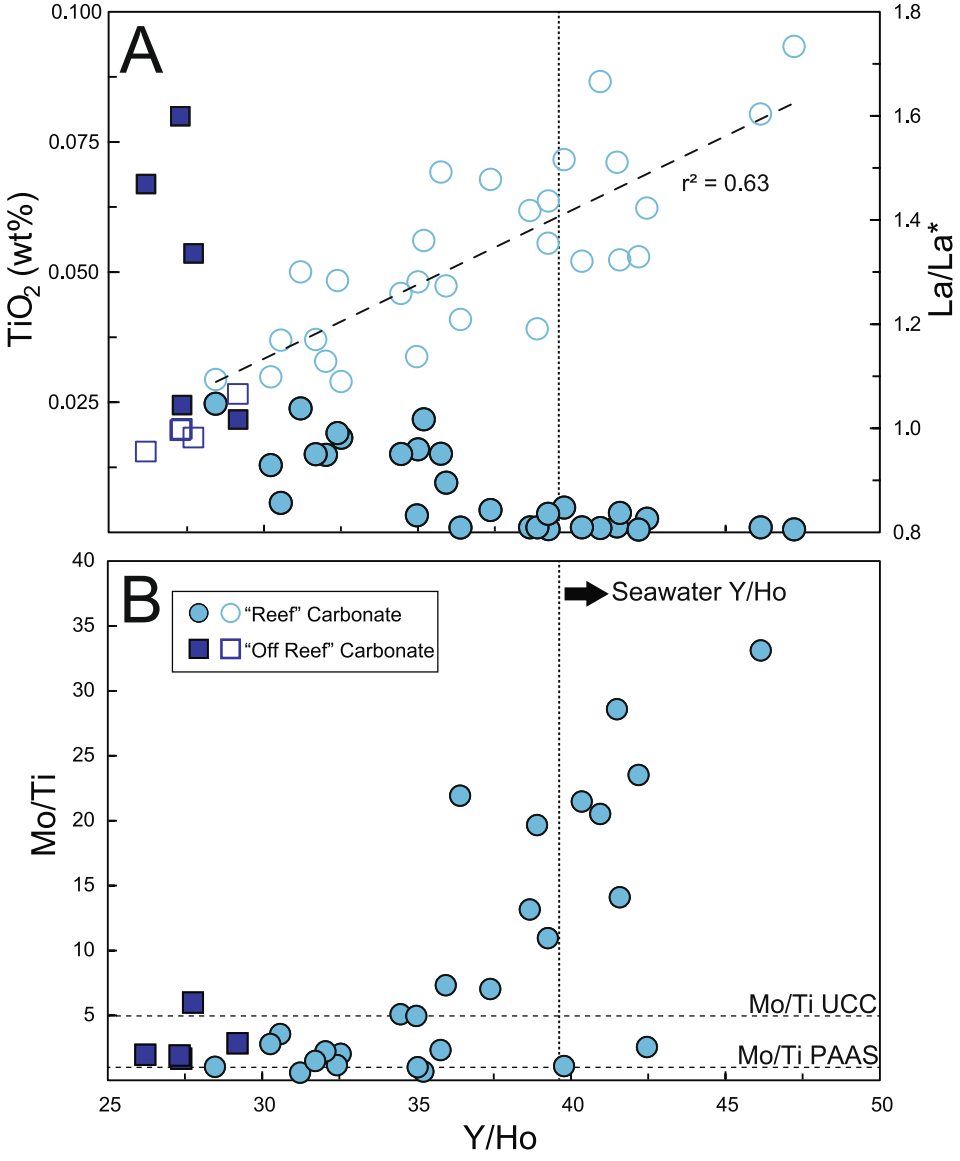

Fig. 6. Influence of detrital input on trace element geochemistry of the reef and off-reef carbonates based on Y/Ho ratio (Sample Set B, data listed in Table 3 of the electronic appendix). All data analysed via solution ICP-MS. **A:** Y/Ho vs. TiO_2 and the La anomaly. Filled symbols refer to Y/Ho vs TiO_2 (primary Y axis), open symbols refer to Y/Ho vs La/La* (secondary Y axis). Positive correlation between Y/Ho and La/La* indicated by the dashed line represents mixing between seawater- and detrital-dominated geochemical signatures, whereas increasing TiO_2 corresponds to increased detrital influence, assuming all Ti derives from continental sources. **B:** Y/Ho covariation with Mo/Ti indicating that the proportion of Mo in the carbonate derived from seawater increases with increasing Y/Ho. Vertical dotted line in both A and B represents minimum Y/Ho ratio typical of modern seawater. Horizontal dotted lines in B indicate Mo/Ti of PAAS and UCC as outlined in Taylor and McLennan (1985) and Rudnick et al. (2003), respectively.

Supplementary Figure S2; S3).

The effect of mixing of trace elements derived from secondary components is demonstrated by the *in-situ* analysed YREE data. Trivalent Ce is the only redox-sensitive REE that is readily oxidized to Ce(IV) in oxic environments and adsorbed primarily to Fe and Mn oxyhydroxides (Bau et al., 1996; Bau and Koschinsky, 2009), depleting the dissolved Ce in ocean water relative to the other REEs, such that recent oxic ocean water possesses a significantly negative (i.e. < 1) Ce anomaly (Ce/Ce* <0.55, as low as 0.05; e.g., Bau et al., 1996; Bau and Koschinsky, 2009). Microbial carbonates have been shown not to significantly fractionate the REEs upon incorporation into Ca-carbonate (Kamber and Webb, 2001; Webb and Kamber, 2000, 2011). However, porewater redox variation may also induce adsorption to, and/or release from diagenetic oxides or detrital material in a similar manner to Mo isotopes, and release of Ce from these components during sample dissolution has been shown to mask negative anomalies and even produce false positive anomalies (Cao et al., 2020; Shields and Stille, 2001; Tostevin et al. 2016; Ward et al. 2019). In contrast to the bulk-analysis data of Sample Set A which show no discernible Ce anomalies (0.92–1.02, Fig. 7), *in situ* analysis of these same carbonate samples, although less precise, reveals largely neutral to negative Ce/Ce* (as low as 0.47), with some very positive Ce/Ce* up to 2.1 identified as impurities based on their MREE enrichment (distinguished by their high "Bell Shaped Index", BSI < 1.5; Martin et al., 2010; Tostevin et al., 2016). This indicates large redox variation within, and between, porewaters of reef and off-reef carbonates.

Referring to the dataset analysed for Mo isotopes (Sample Set B), calculated Ce/Ce* close to unity (0.91–1.05), as well as a good correlation between Ce and Ti concentration and a possible covarying relationship between Ce and Y/Ho (Fig. 7) points towards end-member-mixing between carbonate and continental detritus, rather than desorption from Mn oxides. Nevertheless, a similar mixing relationship between these detrital indicators and Mo is not observed (Supplementary Figure S6), nor is there any significant correlation between Mo and Fe or Mn, or Cu, As or other trace metals which may otherwise indicate incorporation of Mo sourced from Fe or Mn oxides, or sulfides, respectively (Supplementary Figure S6).

5.2.3. *Evaluating the role of recrystallisation*

A final point to note is the so far understudied effect of post-depositional recrystallisation and element mobilisation on the δ^{98}Mo signal of the carbonate during dolomitisation. Low Mg/Ca and Mn/Sr ratios in both reef and off-reef carbonates indicate minimal substitution of these elements, as would be expected during dolomitisation, which commonly involves Mg, Mn and Fe (Fig. 8; Kaufman and Knoll, 1995). The absence of correlation between δ^{13}C and δ^{18}O data indicates

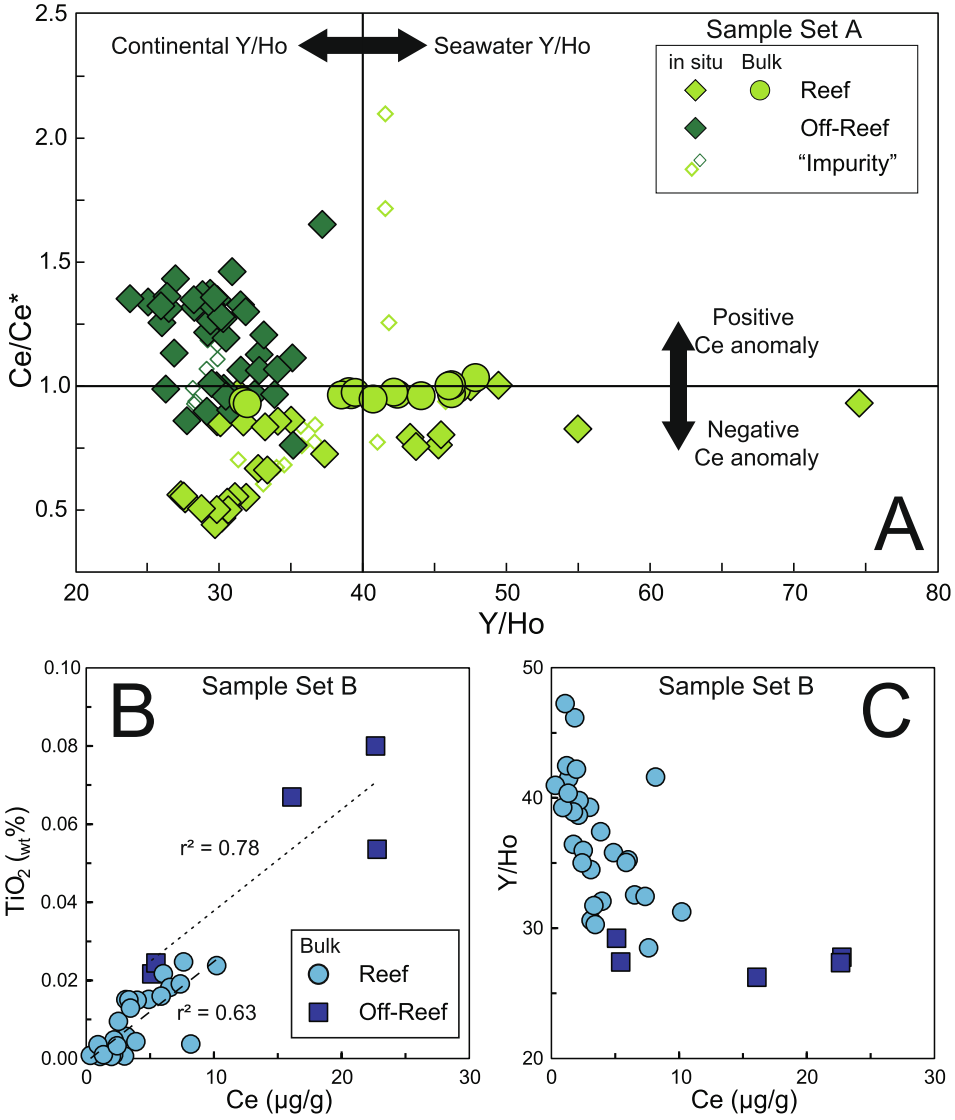

Fig. 7. A: Extent of the Ce anomaly of Sample Set A (Ce/Ce*, as calculated using the method of Lawrence et al., 2006) in the *in situ*-analysed SKF carbonates (diamonds) in comparison to the amount of apparent detrital influence as represented by the Y/Ho ratio. Bulk REE analysis of the same samples represented by circles. Open diamonds represent measurements with BSI>1.5 indicating MREE enrichment, which may skew the Ce anomaly. *In situ* data listed in Table 4. Bulk data reported in Table 3. **B:** Covariation between Ce and Ti concentrations of bulk-digested samples of Sample Set B only (Data listed in Table 3). Dashed and dotted lines and accompanying R^2 values are separate regression lines for reef and off-reef carbonates, respectively. Sample Sets A and B cannot be compared directly and are used for qualitative comparison only.

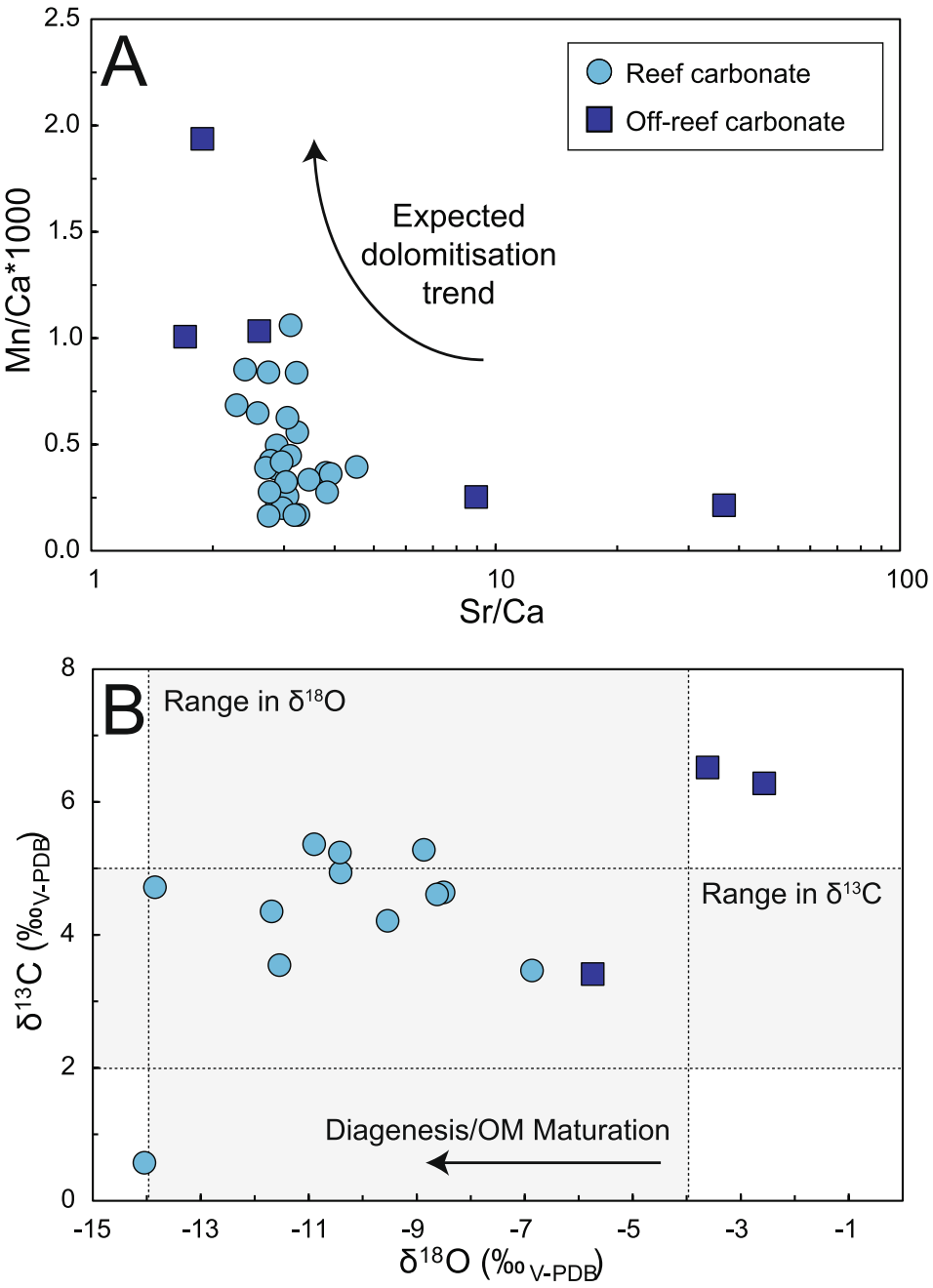

Fig. 8. A: Mn/Ca and Sr/Ca compositions of the SKF carbonates vs. the expected direction of Mn vs Sr evolution during dolomitisation (arrow). **B:** $\delta^{13}C$ and $\delta^{18}O$ compositions of SKF carbonates relative to Peedee Belemnite. Arrow depicts expected trend in $\delta^{18}O$ as a result of diagenesis and organic matter maturation, in which the heaviest values are closest to the original composition. Vertical and horizontal grey bands represent the range in $\delta^{18}O$ and $\delta^{13}C$ of Proterozoic carbonates at 0.85 Ga, respectively, as depicted in Kasting et al. (2006) and Halverson (2006). Individual measurement uncertainties are smaller than symbol size. All samples from Sample Set B, Table 2 and 3.

minimal to no diagenetic resetting of $\delta^{13}C$ (Fig. 8; Halverson, 2006; Kasting et al., 2006; Ling et al., 2013). Voegelin et al. (2010) found no link between dolomitisation and $\delta^{98}Mo$ in mixed limestone and dolomite samples of the Ghaap Group of the Transvaal Supergroup, based on the lack of correlation between $\delta^{98}Mo$ and Mg concentrations ($r^2 = 0.14$) and $\delta^{18}O$ ($r^2 = 0.03$). Such correlations are also not seen here, although this may not be definitive due to analysis of separate sample aliquots. Although minor dolomite is visible in thin section (Supplementary Fig. 2B,C) the geochemical data indicate that it is not pervasive. Thus, there is no indication that dolomitization could have significantly affected carbonate $\delta^{98}Mo$ signatures.

5.2.4. *Assessing carbonate $\delta^{98}Mo$ signatures as estimate of 0.85 Ga seawater*

Although it is clear that secondary components present in the Little Dal carbonate have the potential, and are likely, to cause the observed variation in $\delta^{98}Mo$ and [Mo] data, the precise effect of their inclusion into the bulk $\delta^{98}Mo$ signature remains uncertain within the framework of the current data. Molybdenum isotope fractionation is so far known only to be capable of producing strictly unidirectional isotope effects that only yield $\delta^{98}Mo$ signatures lighter than the initial source; thus the isotopically heaviest sample in a pool may be considered closest to true coeval seawater. This has so far been the conventional method for establishing a minimum estimate of ancient ocean water $\delta^{98}Mo$ compositions and its temporal evolution (see compilations in Kendall et al., 2009; Kurzweil et al., 2015a; and Thoby et al., 2019). The maximum $\delta^{98}Mo$ value of this dataset of 1.64 ‰ as an estimate for seawater at 0.85 Ga might be supported by the fact that 6 samples show similarly isotopically heavy signatures above 1.5 ‰ irrespective of [Mo] and trace element signatures from both the reef and off-reef samples. Furthermore, the variation in $\delta^{98}Mo$ indicates that the inevitable contribution from continental sources, or indeed from oxides, though still

unidentified, is not sufficient to mask the carbonate signature entirely.

5.3. Depositional environment of the Stone Knife Formation

In addition to δ^{98}Mo variability within the carbonate, the current dataset reveals a ~0.4 ‰ difference between the maximum δ^{98}Mo values of carbonate (irrespective of reef or off-reef) and black shale (0.76 – 1.29 ‰) in this study. Despite the differing mechanism of Mo incorporation into both deep-water archives (lime mudstone precipitating in the water column versus organic-rich, Mo-sequestering shale), and their formation in different parts of the water column, the maximum δ^{98}Mo composition should be comparable assuming efficient sequestration of Mo into the shale, i.e., should reflect that of coeval seawater. Although it has been established previously that black shale δ^{98}Mo signatures are susceptible to erroneous estimates owing to undetected non- or weakly-euxinic conditions (e.g., Neubert et al., 2008), the fact that our black shale data are comparatively less variable than our carbonate data (excluding one outlier of 0.3 ‰), and that the maximum value is within the range of many previous estimates of Proterozoic seawater δ^{98}Mo composition derived from shales (1.1–1.4 ‰; Kendall et al., 2009, 2011; Dahl et al., 2011; Gilleaudeau et al., 2020), a discussion is required in the context of probable localised depositional environments, palaeoredox conditions, the dynamics of carbonate depositional systems, and water-column stratification.

Precipitation of lime mud in the oxic upper water column before sinking to the basin floor is indicated already by the striking similarity between the δ^{13}C values between the "deep water" SKF and the stratigraphically equivalent shallow water Boot Inlet Formation (Greenman et al., 2020) in the absence of organic carbon remineralisation in an anoxic environment. This is supported by the YREE pattern of the "cleanest" reef carbonate and off-reef lime mudstone samples of both the bulk- and *in situ*- analysed samples (Fig. 9; indicated by relative ΣREE, Y/Ho and La/La*; Lawrence et al., 2006) which are comparable to those of modern oxidised seawater; namely having a positive La anomaly, a Ce anomaly and superchondritic Y/Ho ≫28 (inset Fig. 9). This pattern arises from the differential removal of REEs from solution during estuarine mixing (Webb and Kamber, 2011) and sorption/desorption cycling through the oceanic water column. The dominantly flat YREE patterns among the other off-reef carbonate samples reflect the variable influx of detrital input, but the pattern is still preserved in samples with the highest Y/Ho ratios (Fig. 7).

A first indication of the palaeoredox conditions of the environment of formation and/or deposition is the Ce anomaly (Ce/Ce*). Ce/Ce* in modern oxidised seawater is as low as 0.06, but consistently lower than

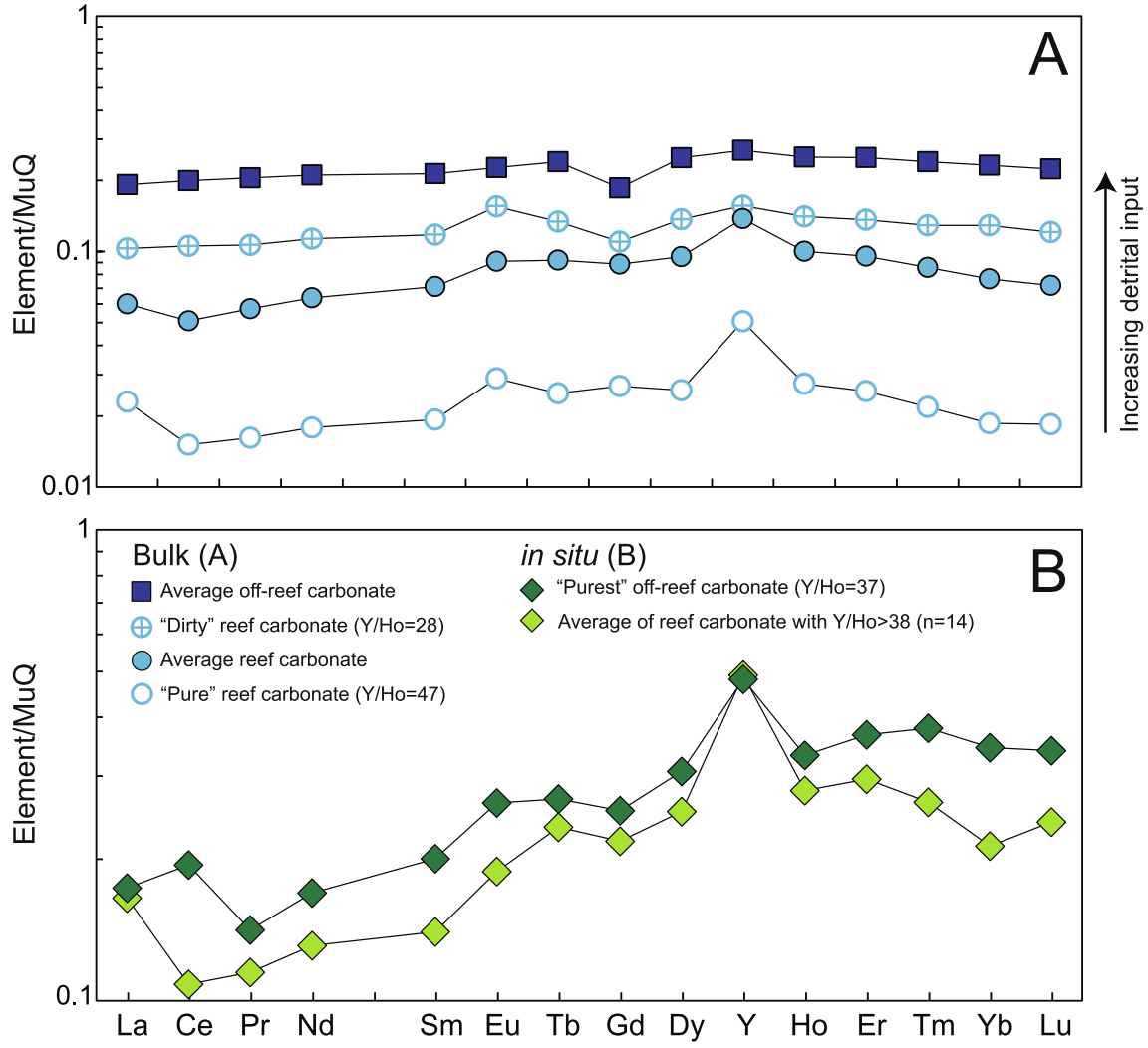

Fig. 9. Yttrium and rare earth element (YREE) diagrams for the SKF carbonates normalised to MuQ (Kamber et al., 2005). **A:** Bulk-digested YREE patterns of Sample Set B showing the progression between samples influenced most heavily by detrital influx to the "purest" carbonate sample based on Y/Ho ratios. Data listed in Table 3. **B:** Comparison of reef and off-reef samples analysed *in situ* from Sample Set A. Data chosen is least affected by detrital influx (i.e., with highest Y/Ho ratios). Data listed in Table 3 and 4.

0.55 (Byrne and Sholkovitz, 1996; Ling et al., 2013) due to the decoupling of Ce from the other REEs upon adsorption and desorption in the water column and leading to a Ce/Ce* value ≪1. In the Archaean, under a largely anoxic atmosphere, Ce/Ce* measured in unaltered microbial carbonates ranges from 0.9 to 1.3 (Kamber et al., 2014). The reef carbonate Ce/Ce^*_{insitu} values here are largely negative (minimum 0.47) indicating that the upper part of the water column in the SKF basin was well oxidised at least in the vicinity of the photosynthesising microbial reefs (Fig. 7; 9). In the deeper-water off-reef facies, significant positive or neutral Ce/Ce* values are evident. Planavsky et al. (2010) attributed rare positive Ce anomalies in Palaeoproterozoic banded iron formations to their precipitation below the redoxcline from anoxic water, consistent with deposition in a stratified water column and indicating active particulate shuttling, whereby Ce-rich Mn oxides that precipitated in the shallow waters were redissolved in the anoxic bottom waters. The resulting Ce/Ce* pattern resembles that observed in the modern stratified Black Sea (German et al., 1991). The low REE content of the off-reef carbonate as well as the lack of a correlation between Ce/Ce^*_{insitu} and Y/Ho (Fig. 7) precludes the derivation of a positive Ce anomaly simply from an influx of terrigenous sediment. Considering that the lime mudstone precipitated in the upper water column before settling in to the basin floor, additional Ce must have been supplied from the deep basin waters and/or porewaters and suggests precipitation of at least some of the carbonate as interstitial cement under suboxic to anoxic seafloor or shallow burial conditions.

In regards to the shale samples, although the organic carbon content is within the range of other Precambrian black shales (e.g., Gilleaudeau et al., 2020; Kendall et al., 2015; Kurzweil et al., 2015a, 2015b; Ostrander et al., 2020; Scott et al., 2008; Wille et al., 2007), as well as marginal parts of modern euxinic basins (e.g., Black Sea margin, Nägler et al., 2005; Neubert et al., 2008), the characteristic redox-sensitive metal enrichment of anoxic to euxinic sediments is lacking or only mildly expressed. Molybdenum concentration is limited (<10 μg/g Mo) and the $Mo_{solnICP}$/TOC is consistently below 1 μg/g per wt%. Enrichment factors calculated for Mo $_{solnICP}$, U, V and Cr relative to MuQ (Kamber et al., 2005; Marx and Kamber 2010) and PAAS (Taylor and McLennan, 1985) are also limited, $Mo_{EF\text{-}PAAS}$ reaching maxima of ~4, in contrast to, for example, the 1.2 Ga euxinic Bijaygarh Shale with Mo_{EF} ranging up to 72 (Gilleaudeau et al., 2020; note: these EFs were calculated using values of UCC in Rudnick et al. (2003), which result in slightly lower EFs than when calculated via PAAS, though are still broadly comparable). This is closer in comparison to modern euxinic sediments such as the Cariaco basin, which has Mo_{EF} of up to and over 200 (Algeo and Tribovillard, 2009). A relatively good covariation between $Mo_{EF\text{-}PAAS}$ and $U_{EF\text{-}PAAS}$ may be diagnostic of redox variation (Fig. 10), but Mo/U_{auth} ratios below 1 (Table 2) favour the uptake of U in ferruginous porewater where Mo is far less affected (e.g., Algeo and Tribovillard, 2009). Finally, coupling the limited Mo and V enrichment with the absence of Cr enrichment ($Cr_{EF\text{-}PAAS}$ ~ 1, Table 2) might be further evidence of the widespread drawdown of the Cr reservoir in a predominantly ferruginous anoxic, non-euxinic basin at 0.85 Ga. In contrast to Mo, which is specifically sensitive to removal in the presence of dissolved H_2S, Cr is

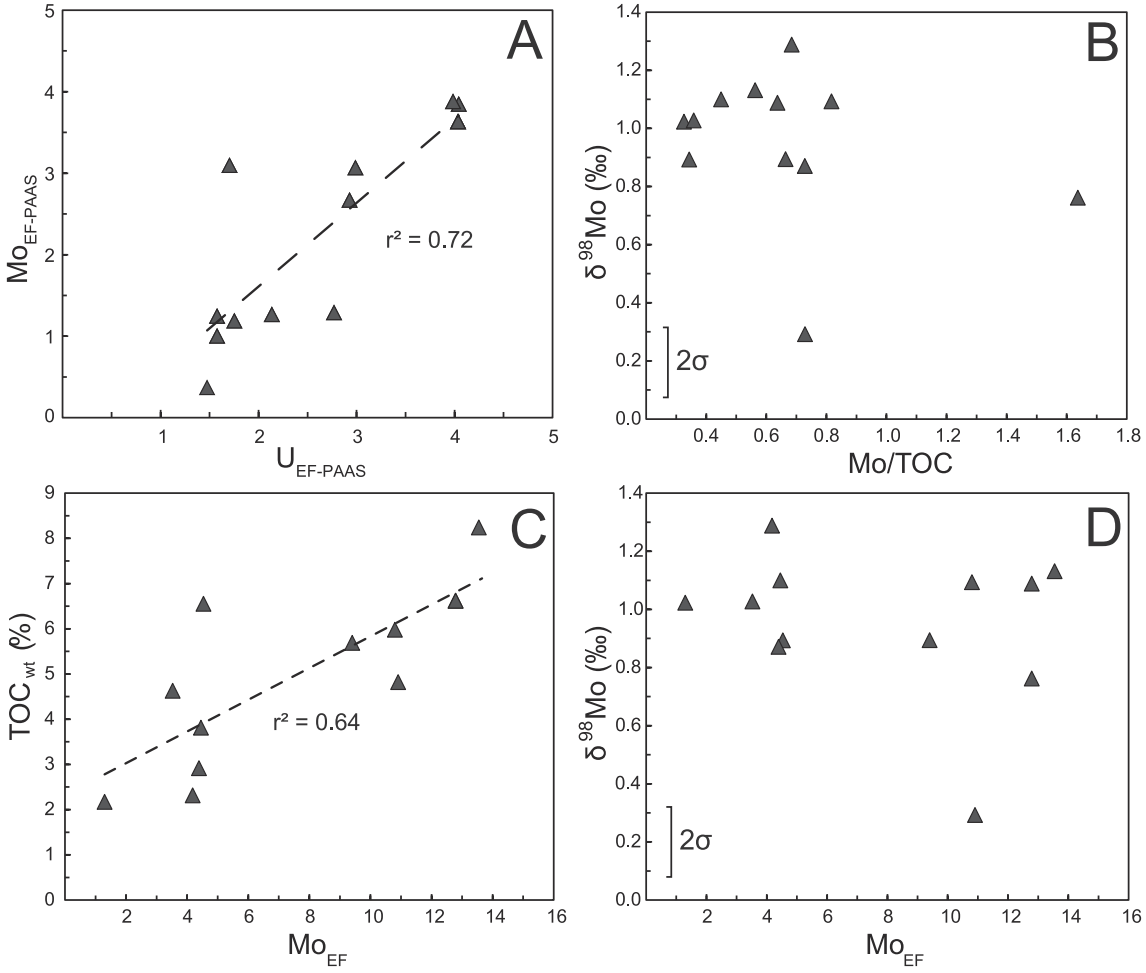

Fig. 10. Covariation between $\delta^{98}Mo$, TOC and enrichment factors (EF) of Mo and U in SKF shales as calculated relative to PAAS. [Mo] reported here and used in EF calculations as analysed via solution ICP-MS. **A:** Mo_{EF} vs U_{EF}, **B:** $\delta^{98}Mo$ vs Mo/TOC, **C:** TOC vs Mo_{EF}, D: $\delta^{98}Mo$ vs Mo_{EF}. 2σ reproducibility in $\delta^{98}Mo$ data is indicated at ±0.12 ‰, individual measurement $2\sigma\bar{x}$ uncertainties are smaller than symbol size. All samples here from Sample Set B and reported in Table 2.

reactive with a variety of reductants leading to its expected enrichment in anoxic environments irrespective of dissolved sulfide content.

One quite obvious explanation of the limited Mo enrichment could be the insufficient or partial conversion of dissolved MoO_4^{2-} to MoS_4^{2-} owing to low porewater levels of dissolved sulfide in non- to weakly-euxinic environments, producing highly fractionated, variable proportions of more to less particle-reactive molybdate species (Nägler et al., 2011; Romaniello et al., 2016). Adsorption of isotopically light $MoO_xS_{4-x}^{2-}$ species in anoxic or weakly-euxinic shale produces sediment with δ^{98}Mo signatures lighter than those of the overlying water column, complicating interpretations of ancient ocean water δ^{98}Mo signatures. Such insufficient uptake would be accompanied by a positive correlation between δ^{98}Mo and Mo/TOC, because more efficient conversion to MoS_4^{2-} promotes the scavenging of Mo and the preservation of the ambient heavy seawater δ^{98}Mo (e.g., Dickson et al., 2016; Duan et al., 2010; Kendall et al., 2015; Ostrander et al., 2020). This relationship is, inauspiciously, also absent here.

The lack of a correlation between $Mo_{solnICP}$/TOC or $Mo_{EF\text{-}MuQ}$ and δ^{98}Mo (Fig. 10) indicates that the isotope composition of the SKF shale is controlled neither by efficiency, or amount, of Mo uptake to the sediment. Instead, Mo_{EF} and $Mo_{solnICP}$/TOC in organic-rich sediment are highly dependent on the basin's Mo supply, displaying specific behaviours based on the degree of basin restriction, where $Mo_{solnICP}$/TOC decreases with increasing basin restriction (Algeo and Lyons, 2006; Nägler et al., 2005, 2011). Our working hypothesis is that the SKF basin was stratified with suboxic to anoxic, ferruginous bottom waters and experienced a degree of bottom-water restriction, particularly during sea-level low stands. Alternatively, the overall marine inventory of Mo (and other redox-sensitive trace metals) may have been lower, leading to apparent lack of enrichments. In this scenario, a final point to consider is the possibility that a highly reduced Mo inventory of the basin water at 0.85 Ga may have permitted quantitative transfer and fixation of Mo to the sediment without the characteristic Mo enrichment or elevated Mo/TOC (Ostrander et al., 2020), allowing the transmission of the seawater δ^{98}Mo signal.

Regardless of its exact reason, one consequence of limited Mo enrichment is the increasing likelihood of a significant influence of the continental component of the shale on the bulk δ^{98}Mo signature, skewing the authigenic component towards lighter values. Although there is no clear mixing between $Mo_{solnICP}$/Al and δ^{98}Mo of the SKF shales, calculation of the fraction of detrital component (f_{det}) in the bulk shale sample compared to the bulk UCC (here using PAAS (Taylor and McLennan, 1985) where [Mo], [Al] and Mo/Al are 1.0 μg/g, 18.9 wt% and 0.05, respectively) via the relationship.

$$f_{det} = \frac{Al_{tot} \times \frac{Mo}{Al\ PAAS}}{Mo_{tot}}$$

where *tot* is the bulk shale sample, indicates values of f_{det} ranging from ~0.1 to ~0.5 (excluding one erroneous sample with Mo/Al of 0.04), assuming a continental detrital composition close to PAAS. The δ^{98}Mo signature of the authigenic shale (*auth*) is then calculated as.

$$\delta_{auth} = \frac{\delta_{tot} - (f_{det} \times \delta_{PAAS})}{1 - f_{det}}$$

where δ is the δ^{98}Mo signature of the bulk shale (*tot*) and detrital component (represented by an estimate of the UCC). Correction becomes exceedingly dependent on the specific parameters used for the detrital component estimate (i.e., Mo/Al and δ^{98}Mo of the assumed detrital component) and becomes highly variable with increasing f_{det} (Ostrander et al., 2020). Estimates of $\delta^{98}Mo_{auth}$ in this study vary in samples with $f_{det} > 0.4$ depending on the value used for $\delta^{98}Mo_{det}$ between 0.00, 0.25 and 0.40 ‰. Estimates for $\delta^{98}Mo_{auth}$ where $f_{det} < 0.4$ are between 0.01 and 0.23 ‰ heavier than $\delta^{98}Mo_{tot}$ (Supplementary Figure S7) with little influence on the choice of $\delta^{98}Mo_{det}$. The correction for detrital influence on the SKF shales increases the δ^{98}Mo signature closer to that expressed by the carbonates, indicating that this discrepancy between the two archives may be in part due to mixing of several Mo sources. The uncertainty in estimating the detrital component composition hinders a robust calculation of $\delta^{98}Mo_{auth}$ and is here used only as an illustration of this effect.

5.4. Implications for the redox state of the Neoproterozoic ocean

So far, all but two published estimates of Proterozoic seawater δ^{98}Mo from black shales have yielded maximum values between 1.11 and 1.38 ‰ for strata between 1.8 and 0.7 Ga (Dahl et al., 2011; Gilleaudeau et al., 2020; Kendall et al., 2009, 2011), several of which (e.g., Gilleaudeau et al., 2020) depict non-euxinic conditions. This is in contrast with the significantly higher black shale estimates of 1.7 ‰ at 1.4 Ga (Diamond et al., 2018) and 2.2 ‰ at 1.56 Ga (Ye et al., 2021). Our maximum seawater δ^{98}Mo estimate of 1.64 ‰ approaches these heavier estimates, as well as that put forward by Baldwin et al. (2013) of up to 1.8 ‰ from the 0.7 Ga stratigraphically younger Rapitan IF, the temporally closest non-shale estimate reported in the literature. Our black shale δ^{98}Mo data, on the other hand, agree more closely with previous black shale data centring around 1.2 ‰. Gilleaudeau et al. (2020) speculated that many previous black shale archives representing ferruginous conditions may have captured the seawater δ^{98}Mo signature in spite of a lack of Mo enrichment on the basis of a dampened Mo inventory. On first interpretation, it may be reasonable to infer a fluctuating δ^{98}Mo composition on a time scale of tens to hundred of m.y. following pulses of oxygenation through the Proterozoic. However, the fact that our contemporaneous shale and carbonate data show a difference in δ^{98}Mo within the same delta range as these two pools of previous estimates, one dominated by shale and the other by non-shale archives, raises the question as to whether this heterogeneity represents genuine oscillations in oxygenation, or artefacts of inter-archive discrepancies.

Similar inconsistencies between broadly time-equivalent carbonate and black shale δ^{98}Mo has been noted in Archaean (Thoby et al., 2019; Voegelin et al., 2010) and Ediacaran (Kurzweil et al., 2015a) samples. Thoby et al. (2019) speculated that the difference between δ^{98}Mo signatures of pre-GOE carbonate and shale lithologies of a similar age may have been influenced by chemical heterogeneity between shallow and deep water settings induced by highly localised oxygen oases, though the authors noted that the long residence time of Mo in comparison to that of waters of a continental platform or shelf (days to years) rendered this scenario difficult to fathom. The Little Dal reefs probably represented localised oxygen-rich upper-water-column environments in the vicinity of photosynthesising microbial reef-builders (Turner, 2021). A definitive chemostratigraphy of the SKF basin δ^{98}Mo composition is not possible to build here, owing to the heterogeneity of the carbonate samples discussed above (provided nonetheless in Supplementary Figure S4) and due to the fact that correlation of the reef and equivalent off-reef carbonates and shales can only be approximated (Supplementary Figures S1 and S4). Nonetheless, the residence time of Mo in the Proterozoic ocean has been estimated to be >30 ky (Dahl et al., 2011); thus, assuming that the ocean circulation was not starkly different from that of today, we infer that the δ^{98}Mo of the seawater δ^{98}Mo in the SKF basin was homogeneously distributed.

Instead, we draw attention to the fact that the 0.4 ‰ difference between the two archives resembles the inconsistency documented in sediment at similar shallow (~100–500 m) depths in the Black and Baltic Seas, where shallow-water sediments have a δ^{98}Mo composition ~0.5 ‰ lighter than the overlying water column (Algeo and Lyons, 2006; Nägler et al., 2005, 2011). In general, these authors inferred fractionation between the anoxic lower water column and sediment of ~0.5 ± 0.3 ‰, but far greater (up to 2.3 ‰) above the redoxcline. Furthermore, we have demonstrated the effect of the significant influence of the detrital Mo source within shale, contributing to the likely lowered δ^{98}Mo signature. Within this framework, and considering the geochemical evidence indicating that the SKF shales are unlikely to have

captured seawater δ^{98}Mo signatures, it is reasonable to assume that a similar offset is seen between the two contemporaneous archives of this study. We therefore propose that the Little Dal carbonate is the more reliable representative of the minimum seawater δ^{98}Mo composition at 0.85 Ga, of 1.64 ‰.

The question then remains as to whether the temporally variable estimates within the collective literature δ^{98}Mo estimates of the Proterozoic ocean are accurate, indicating a rapidly fluctuating and/or heterogeneous ocean redox state, or are alternatively an erratic artefact of depositional conditions akin to the above suggested scenario for the SKF basin. Transient changes in redox conditions and increases in oxygenation have been suggested in several recent studies (Diamond et al., 2018; Planavsky et al., 2018). Kurzweil et al. (2015a) argued that unlike the modern ocean, δ^{98}Mo in Precambrian to Cambrian times was neither spatially nor temporally uniform, and that short-term heavy δ^{98}Mo records do not necessarily imply global oxygenation, but in some cases reflect short-term and/or localised fluctuations in environmental conditions. A hypothesis following from this could be that δ^{98}Mo compositions recorded by the 0.85 Ga SKF carbonates, as well as the 1.5–1.6 Ga carbonates of Luo et al. (2021), 1.4 Ga euxinic black shale unit of Diamond et al., (2018) and 0.7 Ga BIFs of Baldwin et al., (2013) represent transient expansions of the oxic Mo sink during these times. However, this hypothesis would require critical assumptions: 1) that the offset between Little Dal carbonate and shale is an artefact of Mo removal and fractionation in a non-euxinic setting specific to the depositional environment of the SKF basin, with the black shales being less reliable then the carbonates, and 2) that the previously determined Proterozoic seawater δ^{98}Mo derived from euxinic and non-euxinic black shales (e.g., Arnold et al., 2004; Dahl et al., 2011; Gilleaudeau et al., 2020; Kendall et al., 2009, 2011) are indeed faithful records, in contrast to the SKF shale values.

Although it is plausible that the balance between sources and sinks of Mo (and therefore the Mo residence time) may have shifted in response to fluctuating and/or spatially heterogeneous oxygen levels over time scales of hundreds of m.y., it cannot be ignored that even restricted modern euxinic black shales can depict an offset between sediment and seawater δ^{98}Mo values. The question is then raised as to whether some, or all previously analysed Proterozoic shales are also systematically shifted from their respective seawater values, regardless of redox conditions, thereby underestimating the δ^{98}Mo value of seawater throughout the Proterozoic (Gilleaudeau et al., 2020). Until the apparent transient shifts in ocean δ^{98}Mo can be definitively distinguished from inter-proxy or inter-archive discrepancies, we propose that the Proterozoic ocean δ^{98}Mo was more stable than is currently portrayed, and was closer to the heavier of the currently available δ^{98}Mo estimates. Finally, this scenario would then imply that the most significant rise in oxygenation occurred later in the Neoproterozoic, sometime after 0.85 Ga.

6. Conclusions

Reconstructing the Mo isotope composition of the Proterozoic ocean presents a challenge due to the relative dearth of suitably preserved archives as well as a high dependence of geochemical tools on specific depositional environments. Previous Mo isotope data obtained from black shales initially supported the view that the size of the Mo oxic sink remained stable through the Proterozoic. However, the inclusion of non-shale archives in these collective studies has complicated this interpretation, suggesting instead a spatially heterogeneous and fluctuating redox state of the Neoproterozoic ocean. This study reports, and evaluates the use of, δ^{98}Mo compositions as well as major and trace element data of two contemporaneous archives (shallow-water microbial carbonates and coeval deep-water lime mudstones, and black shales) of the 0.85 Ga mid-Neoproterozoic Stone Knife Formation (SKF), Little Dal Group, Mackenzie Mountains, deposited in an intracratonic basin just prior to the possible onset of the NOE.

Reef carbonate U-Pb isotope data of the SKF show variably uranogenic Pb isotopes in the absence of elevated thorogenic Pb, supporting delivery of soluble hexavalent U from weathering of land under oxic conditions. The resulting isochron indicate a depositional age of 0.845 ± 0.028 Ga, possibly near the beginning of the Neoproterozoic oxygenation event, filling a temporal gap in Mo isotope data between 1.2 Ga and the Cryogenian.

By analogy with many earlier studies, the isotopically heaviest δ^{98}Mo value of 1.64 ‰ recorded in the shallow-water reef microbial carbonate is here regarded as the closest approximation of ambient seawater at 0.85 Ga, though the true seawater value was probably even more positive. Trace element analysis indicates variable effects of secondary mineral formation and detrital input as is expected for microbial carbonates. The contemporaneous black shales deposited in deeper water are isotopically not as heavy (maximum δ^{98}Mo 1.29 ‰, similar to previously reported Proterozoic black shales), yielding a discrepancy of ~ 0.4 ‰. However, geochemical analysis suggests that at times in the Precambrian, black shales may not be a suitable proxy for coeval seawater Mo isotope composition.

Instead, we note here that this discrepancy resembles the fractionation previously documented between modern euxinic black shales and overlying water column (e.g., Black Sea). Considering that Proterozoic ocean δ^{98}Mo estimates derived from non-shale archives are consistently isotopically heavier than those derived from black shale, regardless of interpreted depositional environment (euxinic vs. non-euxinic), we propose that previous estimates of Proterozoic ocean water δ^{98}Mo compositions have been underestimated, and true ocean water δ^{98}Mo is closer to the 'heavier' estimates derived from non-shale archives. If this pattern is valid, it is permissible to infer that the magnitude of the Mo oxic sink may have remained relatively stable throughout the Proterozoic, closer to the heavier δ^{98}Mo bounds of the range of reported estimates, with its expansion occurring sometime after 0.85 Ga.

CRediT authorship contribution statement

E.M. O'Sullivan: Methodology, Validation, Formal analysis, Investigation, Writing – original draft, Visualization. **T.F. Nägler:** Conceptualization, Methodology, Validation, Resources, Writing – review & editing, Supervision, Project administration, Funding acquisition. **E.C. Turner:** Conceptualization, Methodology, Formal analysis, Investigation, Resources, Writing – review & editing, Visualization. **B.S. Kamber:** Conceptualization, Methodology, Formal analysis, Investigation, Resources, Writing – review & editing. **M.G. Babechuk:** Writing – review & editing. **S.P. O'Hare:** Writing – review & editing.

Declaration of Competing Interest

The authors declare that they have no known competing financial interests or personal relationships that could have appeared to influence the work reported in this paper.

Acknowledgements

This research was supported financially by the Swiss National Science Foundation (grant #160034), and in part through a Hochschulstiftung der Burgergemeinde Bern supporting grant. Field work and sample collection by E.C. Turner between 1992 and 2009 under a series of NSERC (Canada) Discovery Grants, all required science and land-access licences, permits, and permissions, and logistical support from Northwest Territories Geological Survey (2009). Special thanks to Cora McKenna at Trinity College Dublin, and to Daniel Rufer, Julijana Gajic and Alannah Brett at the Institute of Geological Sciences, University of Bern for support in sample preparation and analysis. Thanks also to Martin Wille at the University of Bern for conceptualisation, scientific input and assistance with manuscript preparation. We would also like to extend our thanks to the two anonymous reviewers who provided

constructive and positive feedback to this work, as well as editors Frances Westall and Marly Babinski for editorial handling of this manuscript.

Appendix A. Supplementary material

Supplementary data to this article can be found online at https://doi.org/10.1016/j.precamres.2022.106760.

References

Aitken, J., 1981. Stratigraphy and sedimentology of the Upper Proterozoic Little Dal Group, Mackenzie Mountains, Northwest Territories. Proterozoic basins of Canada. Edited by FHA Campbell. Geol. Surv. Can. Pap. 8, 1–10.

Algeo, T.J., Lyons, T.W., 2006. Mo–total organic carbon covariation in modern anoxic marine environments: Implications for analysis of paleoredox and paleohydrographic conditions. Paleoceanography 21.

Algeo, T.J., Tribovillard, N., 2009. Environmental analysis of paleoceanographic systems based on molybdenum–uranium covariation. Chem. Geol. 268 (3-4), 211–225.

Archer, C., Vance, D., 2008. The isotopic signature of the global riverine molybdenum flux and anoxia in the ancient oceans. Nature Geosci. 1, 597–600. https://doi.org/10.1038/ngeo282.

Arnold, G.L., Anbar, A.D., Barling, J., Lyons, T.W., 2004. Molybdenum Isotope Evidence for Widespread Anoxia in Mid-Proterozoic Oceans. Science 304 (5667), 87–90.

Arnórsson, S., Óskarsson, N., 2007. Molybdenum and tungsten in volcanic rocks and in surface and <100°C ground waters in Iceland. Geochim. Cosmochim. Acta 71, 284–304.

Baldwin, G.J., Nägler, T.F., Greber, N.D., Turner, E.C., Kamber, B.S., 2013. Mo isotopic composition of the mid-Neoproterozoic ocean: an iron formation perspective. Precambr. Res. 230, 168–178.

Baldwin, G.J., Turner, E.C., Kamber, B.S., 2016. Tectonic controls on distribution and stratigraphy of the Cryogenian Rapitan iron formation, northwestern Canada. Precambr. Res. 278, 303–322.

Barling, J., Arnold, G.L., Anbar, A.D., 2001. Natural mass-dependent variations in the isotopic composition of molybdenum. Earth Planet. Sci. Lett. 193 (3-4), 447–457.

Barling, J., Anbar, A.D., 2004. Molybdenum isotope fractionation during adsorption by manganese oxides. Earth Planet. Sci. Lett. 217 (3-4), 315–329.

Batten, K.L., Narbonne, G.M., James, N.P., 2004. Paleoenvironments and growth of early Neoproterozoic calcimicrobial reefs: platformal Little Dal Group, northwestern Canada. Precambr. Res. 133, 249–269.

Bau, M., Koschinsky, A., 2009. Oxidative scavenging of cerium on hydrous Fe oxide: evidence from the distribution of rare earth elements and yttrium between Fe oxides and Mn oxides in hydrogenetic ferromanganese crusts. Geochem. J. 43 (1), 37–47.

Bau, M., Koschinsky, A., Dulski, P., Hein, J.R., 1996. Comparison of the partitioning behaviours of yttrium, rare earth elements, and titanium between hydrogenetic marine ferromanganese crusts and seawater. Geochim. Cosmochim. Acta 60 (10), 1709–1725.

Brocks, J.J., Love, G.D., Summons, R.E., Knoll, A.H., Logan, G.A., Bowden, S.A., 2005. Biomarker evidence for green and purple sulphur bacteria in a stratified Palaeoproterozoic sea. Nature 437 (7060), 866–870.

Byrne, R., Sholkovitz, E., 1996. Marine chemistry and geochemistry of the lanthanides. Handbook Phys. Chem. Rare Earths 23, 497–593.

Cabioch, G., Camoin, G., Webb, G.E., Le Cornec, F., Garcia Molina, M., Pierre, C., Joachimski, M.M., 2006. Contribution of microbialites to the development of coral reefs during the last deglacial period: Case study from Vanuatu (South-West Pacific). Sed. Geol. 185 (3-4), 297–318.

Canfield, D.E., 1998. A new model for Proterozoic ocean chemistry. Nature 396 (6710), 450–453.

Canfield, D.E., Poulton, S.W., Knoll, A.H., Narbonne, G.M., Ross, G., Goldberg, T., Strauss, H., 2008. Ferruginous Conditions Dominated Later Neoproterozoic Deep-Water Chemistry. Science 321 (5891), 949–952.

Canfield, D.E., Zhang, S., Frank, A.B., Wang, X., Wang, H., Su, J., Ye, Y., Frei, R., 2018. Highly fractionated chromium isotopes in Mesoproterozoic-aged shales and atmospheric oxygen. Nat. Commun. 9 (1), 1–11.

Cao, C., Liu, X.-M., Bataille, C.P., Liu, C., 2020. What do Ce anomalies in marine carbonates really mean? A perspective from leaching experiments. Chem. Geol. 532, 119413. https://doi.org/10.1016/j.chemgeo.2019.119413.

Chen, X., Li, M., Sperling, E.A., Zhang, T., Zong, K., Liu, Y., Shen, Y., 2020. Mesoproterozoic paleo-redox changes during 1500–1400 Ma in the Yanshan Basin, North China. Precam. Res. 347, 105835.

Chen, X., Romaniello, S.J., Anbar, A.D., 2021. Preliminary exploration of molybdenum isotope fractionation during coprecipitation of molybdate with abiotic and microbial calcite. Chem. Geol. 566, 120102. https://doi.org/10.1016/j.chemgeo.2021.120102.

Cheng, M., Li, C., Chen, X.i., Zhou, L., Algeo, T.J., Ling, H.-F., Feng, L.-J., Jin, C.-S., 2018. Delayed Neoproterozoic oceanic oxygenation: Evidence from Mo isotopes of the Cryogenian Datangpo Formation. Precambr. Res. 319, 187–197.

Clarkson, M.O., Müsing, K., Andersen, M.B., Vance, D., 2020. Examining pelagic carbonate-rich sediments as an archive for authigenic uranium and molybdenum isotopes using reductive cleaning and leaching experiments. Chem. Geol. 539, 119412. https://doi.org/10.1016/j.chemgeo.2019.119412.

Collier, R.W., 1985. Molybdenum in the Northeast Pacific Ocean. Limnol. Oceanogr. 30, 1351–1354.

Czaja, A.D., Johnson, C.M., Roden, E.E., Beard, B.L., Voegelin, A.R., Nägler, T.F., Beukes, N.J., Wille, M., 2012. Evidence for free oxygen in the Neoarchean ocean based on coupled iron–molybdenum isotope fractionation. Geochim. Cosmochim. Acta 86, 118–137.

Dahl, T.W., Canfield, D.E., Rosing, M.T., Frei, R.E., Gordon, G.W., Knoll, A.H., Anbar, A.D., 2011. Molybdenum evidence for expansive sulfidic water masses in ~ 750 Ma oceans. Earth Planet. Sci. Lett. 311 (3-4), 264–274.

Dickson, J.A.D., 1965. A modified staining technique for carbonates in thin section. Nature 205 (4971).

Dickson, A.J., Jenkyns, H.C., Porcelli, D., van den Boorn, S., Idiz, E., 2016. Basin-scale controls on the molybdenum-isotope composition of seawater during Oceanic Anoxic Event 2 (Late Cretaceous). Geochim. Cosmochim. Acta 178, 291–306.

Diamond, C.W., Planavsky, N.J., Wang, C., Lyons, T.W., 2018. What the~ 1.4 Ga Xiamaling Formation can and cannot tell us about the mid-Proterozoic ocean. Geobiology 16 (3), 219–236.

Duan, Y., Anbar, A.D., Arnold, G.L., Lyons, T.W., Gordon, G.W., Kendall, B., 2010. Molybdenum isotope evidence for mild environmental oxygenation before the Great Oxidation Event. Geochim. Cosmochim. Acta 74 (23), 6655–6668.

Erickson, B.E., Helz, G.R., 2000. Molybdenum(VI) speciation in sulfidic waters: Stability and lability of thiomolybdates. Geochim. Cosmochim. Acta 64 (7), 1149–1158.

Eroglu, S., Schoenberg, R., Wille, M., Beukes, N., Taubald, H., 2015. Geochemical stratigraphy, sedimentology, and Mo isotope systematics of the ca. 2.58–2.50 Ga-old Transvaal Supergroup carbonate platform, South Africa. Precam. Res. 266, 27–46.

Farquhar, J., Bao, H., Thiemens, M., 2000. Atmospheric influence of Earth's earliest sulfur cycle. Science 289 (5480), 756–758.

German, C.R., Holliday, B.P., Elderfield, H., 1991. Redox cycling of rare earth elements in the suboxic zone of the Black Sea. Geochim. Cosmochim. Acta 55 (12), 3553–3558.

Gilleaudeau, G.J., Sahoo, S.K., Ostrander, C.M., Owens, J.D., Poulton, S.W., Lyons, T.W., Anbar, A.D., 2020. Molybdenum isotope and trace metal signals in an iron-rich Mesoproterozoic ocean: A snapshot from the Vindhyan Basin, India. Precambr. Res. 343, 105718. https://doi.org/10.1016/j.precamres.2020.105718.

Goldberg, S., Forster, H.S., Godfrey, C.L., 1996. Molybdenum adsorption on oxides, clay minerals, and soils. Soil Sci. Soc. Am. J. 60 (2), 425–432.

Goldberg, S., Forster, H.S., 1998. Factors affecting molybdenum adsorption by soils and minerals. Soil Sci. 163 (2), 109–114.

Goldberg, T., Archer, C., Vance, D., Poulton, S.W., 2009. Mo isotope fractionation during adsorption to Fe (oxyhydr)oxides. Geochim. Cosmochim. Acta 73 (21), 6502–6516.

Goto, K.T., Sekine, Y., Ito, T., Suzuki, K., Anbar, A.D., Gordon, G.W., Harigane, Y., Maruoka, T., Shimoda, G., Kashiwabara, T., Takaya, Y., 2021. Progressive ocean oxygenation at~ 2.2 Ga inferred from geochemistry and molybdenum isotopes of the Nsuta Mn deposit. Ghana. Chemical Geology, 120116.

Greaney, A.T., Rudnick, R.L., Gaschnig, R.M., Whalen, J.B., Luais, B., Clemens, J.D., 2018. Geochemistry of molybdenum in the continental crust. Geochim. Cosmochim. Acta 238, 36–54.

Greber, N.D., Pettke, T., Nägler, T.F., 2014. Magmatic–hydrothermal molybdenum isotope fractionation and its relevance to the igneous crustal signature. Lithos 190-191, 104–110.

Greber, N.D., Puchtel, I.S., Nägler, T.F., Mezger, K., 2015. Komatiites constrain molybdenum isotope composition of the Earth's mantle. Earth Planet. Sci. Lett. 421, 129–138.

Greenman, J.W., Rainbird, R.H., Turner, E.C., 2020. High-resolution correlation between contrasting early Tonian carbonate successions in NW Canada highlights pronounced global carbon isotope variations. Precambr. Res. 346, 105816. https://doi.org/10.1016/j.precamres.2020.105816.

Halverson, G.P., 2006. A Neoproterozoic Chronology. In: Xiao, S., Kaufman, A.J. (Eds.), Topics in GeobiologyNeoproterozoic Geobiology and Paleobiology. Springer Netherlands, Dordrecht, pp. 231–271.

Helz, G.R., Bura-Nakić, E., Mikac, N., Ciglenečki, I., 2011. New model for molybdenum behavior in euxinic waters. Chem. Geol. 284 (3-4), 323–332.

Hoffman, P.F., Li, Z.-X., 2009. A palaeogeographic context for Neoproterozoic glaciation. Palaeogeogr. Palaeoclimatol. Palaeoecol. 277 (3-4), 158–172.

Holland, H.D., 2006. The oxygenation of the atmosphere and oceans. Philos. Trans. Royal Soc. Lond. B: Biol. Sci. 361 (1470), 903–915.

Johnson, J.E., Gerpheide, A., Lamb, M.P., Fischer, W.W., 2014. O_2 constraints from Paleoproterozoic detrital pyrite and uraninite. Bulletin 126 (5-6), 813–830.

Kamber, B.S., Bolhar, R., Webb, G.E., 2004. Geochemistry of late Archaean stromatolites from Zimbabwe: evidence for microbial life in restricted epicontinental seas. Precambr. Res. 132 (4), 379–399.

Kamber, B.S., Greig, A., Collerson, K.D., 2005. A new estimate for the composition of weathered young upper continental crust from alluvial sediments, Queensland, Australia. Geochim. Cosmochim. Acta 69 (4), 1041–1058.

Kamber, B.S., Webb, G.E., 2001. The geochemistry of late Archaean microbial carbonate: implications for ocean chemistry and continental erosion history. Geochim. Cosmochim. Acta 65 (15), 2509–2525.

Kamber, B.S., Webb, G.E., Gallagher, M., 2014. The rare earth element signal in Archaean microbial carbonate: information on ocean redox and biogenicity. J. Geol. Soc. 171 (6), 745–763.

Kashiwabara, T., Takahashi, Y., Tanimizu, M., Usui, A., 2011. Molecular-scale mechanisms of distribution and isotopic fractionation of molybdenum between seawater and ferromanganese oxides. Geochim. Cosmochim. Acta 75 (19), 5762–5784.

Kasting, J.F., Howard, M.T., Wallmann, K., Veizer, J., Shields, G., Jaffrés, J., 2006. Paleoclimates, ocean depth, and the oxygen isotopic composition of seawater. Earth Planet. Sci. Lett. 252 (1-2), 82–93.

Kaufman, A., Knoll, A., 1995. Neoproterozoic variations in the C-isotopic composition of seawater: stratigraphic and biogeochemical implications. Precambr. Res. 73 (1-4), 27–49.
Kendall, B., Creaser, R.A., Gordon, G.W., Anbar, A.D., 2009. Re–Os and Mo isotope systematics of black shales from the Middle Proterozoic Velkerri and Wollogorang formations, McArthur Basin, northern Australia. Geochim. Cosmochim. Acta 73 (9), 2534–2558.
Kendall, B., Gordon, G.W., Poulton, S.W., Anbar, A.D., 2011. Molybdenum isotope constraints on the extent of late Paleoproterozoic ocean euxinia. Earth Planet. Sci. Lett. 307 (3-4), 450–460.
Kendall, B., Komiya, T., Lyons, T.W., Bates, S.M., Gordon, G.W., Romaniello, S.J., Jiang, G., Creaser, R.A., Xiao, S., McFadden, K., Sawaki, Y., Tahata, M., Shu, D., Han, J., Li, Y., Chu, X., Anbar, A.D., 2015. Uranium and molybdenum isotope evidence for an episode of widespread ocean oxygenation during the late Ediacaran Period. Geochim. Cosmochim. Acta 156, 173–193.
Krause, A.J., Mills, B.J., Zhang, S., Planavsky, N.J., Lenton, T.M., Poulton, S.W., 2018. Stepwise oxygenation of the Paleozoic atmosphere. Nat. Commun. 9 (1), 1–10.
Kurzweil, F., Drost, K., Pašava, J., Wille, M., Taubald, H., Schoeckle, D., Schoenberg, R., 2015a. Coupled sulfur, iron and molybdenum isotope data from black shales of the Teplá-Barrandian unit argue against deep ocean oxygenation during the Ediacaran. Geochim. Cosmochim. Acta 171, 121–142.
Kurzweil, F., Wille, M., Schoenberg, R., Taubald, H., Van Kranendonk, M.J., 2015b. Continuously increasing δ^{98}Mo values in Neoarchean black shales and iron formations from the Hamersley Basin. Geochim. Cosmochim. Acta 164, 523–542.
Lawrence, M.G., Jupiter, S.D., Kamber, B.S., 2006. Aquatic geochemistry of the rare earth elements and yttrium in the Pioneer River catchment, Australia. Mar. Freshw. Res. 57 (7), 725. https://doi.org/10.1071/MF05229.
Lawrence, M.G., Kamber, B.S., 2006. The behaviour of the rare earth elements during estuarine mixing—revisited. Mar. Chem. 100 (1-2), 147–161.
Li, Z.X., Bogdanova, S.V., Collins, A.S., Davidson, A., De Waele, B., Ernst, R.E., Fitzsimons, I.C.W., Fuck, R.A., Gladkochub, D.P., Jacobs, J., Karlstrom, K.E., Lu, S., Natapov, L.M., Pease, V., Pisarevsky, S.A., Thrane, K., Vernikovsky, V., 2008. Assembly, configuration, and break-up history of Rodinia: A synthesis. Precambr. Res. 160 (1-2), 179–210.
Ling, H.-F., Chen, X.i., Li, D.a., Wang, D., Shields-Zhou, G.A., Zhu, M., 2013. Cerium anomaly variations in Ediacaran–earliest Cambrian carbonates from the Yangtze Gorges area, South China: Implications for oxygenation of coeval shallow seawater. Precambr. Res. 225, 110–127.
Liu, J.-H., Zhou, L., Algeo, T.J., Wang, X.-C., Wang, Q., Wang, Y., Chen, M.-L., 2020. Molybdenum isotopic behavior during intense weathering of basalt on Hainan Island, South China. Geochim. Cosmochim. Acta 287, 180–204.
Liu, X.M., Kah, L.C., Knoll, A.H., Cui, H., Wang, C., Bekker, A., Hazen, R.M., 2021. A persistently low level of atmospheric oxygen in Earth's middle age. Nat. Commun. 12 (1), 1–7.
Long, D.G.F., Turner, E.C., 2012. Formal definition of the Neoproterozoic Mackenzie Mountains Supergroup (Northwest Territories), and formal stratigraphic nomenclature for terrigenous clastic units of the Katherine Group. Geological Survey of Canada, Open File 7113 40. https://doi.org/10.4095/292168.
Luo, J., Long, X., Bowyer, F.T., Mills, B.J.W., Li, J., Xiong, Y., Zhu, X., Zhang, K., Poulton, S.W., 2021. Pulsed oxygenation events drove progressive oxygenation of the early Mesoproterozoic ocean. Earth Planet. Sci. Lett. 559, 116754. https://doi.org/10.1016/j.epsl.2021.116754.
Lutfi Firdaus, M., Norisuye, K., Nakagawa, Y., Nakatsuka, S., Sohrin, Y., 2008. Dissolved and labile particulate Zr, Hf, Nb, Ta, Mo and W in the western North Pacific Ocean. J. Oceanogr. 64 (2), 247–257.
Lyons, T.W., Reinhard, C.T., Planavsky, N.J., 2014. The rise of oxygen in Earth's early ocean and atmosphere. Nature 506 (7488), 307–315.
Lyons, T.W., Diamond, C.W., Planavsky, N.J., Reinhard, C.T., Li, C., 2021. Oxygenation, life, and the planetary system during Earth's middle history: An overview. Astrobiology 21 (8), 906–923.
Martin, E.E., Blair, S.W., Kamenov, G.D., Scher, H.D., Bourbon, E., Basak, C., Newkirk, D. N., 2010. Extraction of Nd isotopes from bulk deep sea sediments for paleoceanographic studies on Cenozoic time scales. Chem. Geol. 269 (3-4), 414–431.
Marx, S.K., Kamber, B.S., 2010. Trace-element systematics of sediments in the Murray-Darling Basin, Australia: Sediment provenance and palaeoclimate implications of fine scale chemical heterogeneity. Appl. Geochem. 25 (8), 1221–1237.
Mezger, K., Cosca, M.A., 1999. The thermal history of the Eastern Ghats Belt (India) as revealed by U-Pb and ^{40}Ar/^{39}Ar dating of metamorphic and magmatic minerals: implications for the SWEAT correlation. Precambr. Res. 94 (3-4), 251–271.
Miller, C.A., Peucker-Ehrenbrink, B., Walker, B.D., Marcantonio, F., 2011. Re-assessing the surface cycling of molybdenum and rhenium. Geochim. Cosmochim. Acta 75 (22), 7146–7179.
Mills, D.B., Canfield, D.E., 2014. Oxygen and animal evolution: Did a rise of atmospheric oxygen "trigger" the origin of animals? BioEssays 36 (12), 1145–1155.
Milton, J.E., Hickey, K.A., Gleeson, S.A., Friedman, R.M., 2017. New U-Pb constraints on the age of the Little Dal Basalts and Gunbarrel-related volcanism in Rodinia. Precambr. Res. 296, 168–180.
Mukherjee, I., Large, R.R., Corkrey, R., Danyushevsky, L.V., 2018. The Boring Billion, a slingshot for complex life on Earth. Sci. Rep. 8 (1), 1–7.
Nägler, T.F., Anbar, A.D., Archer, C., Goldberg, T., Gordon, G.W., Greber, N.D., Siebert, C., Sohrin, Y., Vance, D., 2014. Proposal for an International Molybdenum Isotope Measurement Standard and Data Representation. Geostand. Geoanal. Res. 38, 149–151.
Nägler, T.F., Neubert, N., Böttcher, M.E., Dellwig, O., Schnetger, B., 2011. Molybdenum isotope fractionation in pelagic euxinia: Evidence from the modern Black and Baltic Seas. Chem. Geol. 289 (1-2), 1–11.
Nägler, T.F., Siebert, C., Lüschen, H., Böttcher, M.E., 2005. Sedimentary Mo isotope record across the Holocene fresh–brackish water transition of the Black Sea. Chem. Geol. 219 (1-4), 283–295.
Nakagawa, Y., Takano, S., Firdaus, M.L., Norisuye, K., Hirata, T., Vance, D., Sohrin, Y., 2012. The molybdenum isotopic composition of the modern ocean. Geochem. J. 46 (2), 131–141.
Neubert, N., Nägler, T.F., Böttcher, M.E., 2008. Sulfidity controls molybdenum isotope fractionation into euxinic sediments: Evidence from the modern Black Sea. Geology 36 (10), 775. https://doi.org/10.1130/G24959A.110.1130/2008201.
Och, L.M., Shields-Zhou, G.A., 2012. The Neoproterozoic oxygenation event: Environmental perturbations and biogeochemical cycling. Earth Sci. Rev. 110 (1-4), 26–57.
Ostrander, C.M., Kendall, B., Olson, S.L., Lyons, T.W., Gordon, G.W., Romaniello, S.J., Zheng, W., Reinhard, C.T., Roy, M., Anbar, A.D., 2020. An expanded shale δ^{98}Mo record permits recurrent shallow marine oxygenation during the Neoarchean. Chem. Geol. 532, 119391. https://doi.org/10.1016/j.chemgeo.2019.119391.
Planavsky, N., Bekker, A., Rouxel, O.J., Kamber, B., Hofmann, A., Knudsen, A., Lyons, T. W., 2010. Rare Earth Element and yttrium compositions of Archean and Paleoproterozoic Fe formations revisited: New perspectives on the significance and mechanisms of deposition. Geochim. Cosmochim. Acta 74 (22), 6387–6405.
Planavsky, N.J., McGoldrick, P., Scott, C.T., Li, C., Reinhard, C.T., Kelly, A.E., Chu, X., Bekker, A., Love, G.D., Lyons, T.W., 2011. Widespread iron-rich conditions in the mid-Proterozoic ocean. Nature 477 (7365), 448–451.
Planavsky, N.J., Reinhard, C.T., Wang, X., Thomson, D., McGoldrick, P., Rainbird, R.H., Johnson, T., Fischer, W.W., Lyons, T.W., 2014. Low Mid-Proterozoic atmospheric oxygen levels and the delayed rise of animals. Science 346 (6209), 635–638.
Planavsky, N.J., Cole, D.B., Reinhard, C.T., Diamond, C., Love, G.D., Luo, G., Zhang, S., Konhauser, K.O., Lyons, T.W., 2016. No evidence for high atmospheric oxygen levels 1,400 million years ago. Proc. Natl. Acad. Sci. 113 (19), E2550–E2551.
Planavsky, N.J., Slack, J.F., Cannon, W.F., O'Connell, B., Isson, T.T., Asael, D., Jackson, J.C., Hardisty, D.S., Lyons, T.W., Bekker, A., 2018. Evidence for episodic oxygenation in a weakly redox-buffered deep mid-Proterozoic ocean. Chem. Geol. 483, 581–594.
Planavsky, N.J., Reinhard, C.T., Isson, T.T., Ozaki, K., Crockford, P.W., 2020. Large mass-independent oxygen isotope fractionations in mid-proterozoic sediments: Evidence for a low-oxygen atmosphere? Astrobiology 20 (5), 628–636.
Poulton, S.W., Canfield, D.E., 2011. Ferruginous Conditions: A Dominant Feature of the Ocean through Earth's History. Elements 7 (2), 107–112.
Poulton, S.W., Fralick, P.W., Canfield, D.E., 2004. The transition to a sulfidic ocean~ 1.84 billion years ago. Nature 431, 173.
Poulton, S.W., Fralick, P.W., Canfield, D.E., 2010. Spatial variability in oceanic redox structure 1.8 billion years ago. Nat. Geosci. 3 (7), 486–490.
Poulton, S.W., Bekker, A., Cumming, V.M., Zerkle, A.L., Canfield, D.E., Johnston, D.T., 2021. A 200-million-year delay in permanent atmospheric oxygenation. Nature 592 (7853), 232–236.
Pu, J.P., Bowring, S.A., Ramezani, J., Myrow, P., Raub, T.D., Landing, E.d., Mills, A., Hodgin, E., Macdonald, F.A., 2016. Dodging snowballs: Geochronology of the Gaskiers glaciation and the first appearance of the Ediacaran biota. Geology 44 (11), 955–958.
Rainbird, R.H., Rayner, N.M., Hadlari, T., Heaman, L.M., Ielpi, A., Turner, E., MacNaughton, R.B., 2017. Zircon provenance data record lateral extent of pancontinental, early Neoproterozoic rivers and erosional unroofing history of the Grenvillian orogeny. Geol. Soc. Am. Bull. 129, 1408–1423.
Reinhard, C.T., Planavsky, N.J., Robbins, L.J., Partin, C.A., Gill, B.C., Lalonde, S.V., Bekker, A., Konhauser, K.O., Lyons, T.W., 2013. Proterozoic ocean redox and biogeochemical stasis. Proc. Natl. Acad. Sci. 110 (14), 5357–5362.
Romaniello, S.J., Herrmann, A.D., Anbar, A.D., 2016. Syndepositional diagenetic control of molybdenum isotope variations in carbonate sediments from the Bahamas. Chem. Geol. 438, 84–90.
Rooney, A.D., Strauss, J.V., Brandon, A.D., Macdonald, F.A., 2015. A Cryogenian chronology: Two long-lasting synchronous Neoproterozoic glaciations. Geology 43 (5), 459–462.
Rudnick, R.L., Gao, S., Holland, H.D., Turekian, K.K., 2003. Composition of the continental crust. The crust 3, 1–64.
Rye, R., Holland, H.D., 1998. Paleosols and the evolution of atmospheric oxygen: a critical review. Am. J. Sci. 298 (8), 621–672.
Shuster, A.M., Wallace, M.W., van Smeerdijk Hood, A., Jiang, G., 2018. The Tonian Beck Spring Dolomite: Marine dolomitization in a shallow, anoxic sea. Sed. Geol. 368, 83–104.
Scott, C., Lyons, T.W., Bekker, A., Shen, Y., Poulton, S.W., Chu, X., Anbar, A.D., 2008. Tracing the stepwise oxygenation of the Proterozoic ocean. Nature 452 (7186), 456–459.
Shields, G., Stille, P., 2001. Diagenetic constraints on the use of cerium anomalies as palaeoseawater redox proxies: an isotopic and REE study of Cambrian phosphorites. Chem. Geol. 175 (1-2), 29–48.
Siebert, C., Nägler, T.F., Kramers, J.D., 2001. Determination of molybdenum isotope fractionation by double-spike multicollector inductively coupled plasma mass spectrometry. Geochem. Geophys. Geosyst. 2 (7), n/a–n/a.
Siebert, C., Nägler, T.F., von Blanckenburg, F., Kramers, J.D., 2003. Molybdenum isotope records as a potential new proxy for paleoceanography. Earth Planet. Sci. Lett. 211 (1-2), 159–171.
Sperling, E.A., Rooney, A.D., Hays, L., Sergeev, V.N., Vorob'eva, N.G., Sergeeva, N.D., Selby, D., Johnston, D.T., Knoll, A.H., 2014. Redox heterogeneity of subsurface waters in the Mesoproterozoic ocean. Geobiology 12 (5), 373–386.
Taylor, S.R., McLennan, S.M., 1985. The continental crust: Its composition and evolution.

Thoby, M., Konhauser, K.O., Fralick, P.W., Altermann, W., Visscher, P.T., Lalonde, S.V., 2019. Global importance of oxic molybdenum sinks prior to 2.6 Ga revealed by the Mo isotope composition of Precambrian carbonates. Geology 47 (6), 559–562.
Tostevin, R., Shields, G.A., Tarbuck, G.M., He, T., Clarkson, M.O., Wood, R.A., 2016. Effective use of cerium anomalies as a redox proxy in carbonate-dominated marine settings. Chem. Geol. 438, 146–162.
Tostevin, R., Mills, B.J.W., 2020. Reconciling proxy records and models of Earth's oxygenation during the Neoproterozoic and Palaeozoic. Interface focus 10 (4), 20190137. https://doi.org/10.1098/rsfs.2019.0137.
Turner, E.C., 2021. Possible poriferan body fossils in early Neoproterozoic microbial reefs. Nature 596 (7870), 87–91.
Turner, E.C., James, N.P., Narbonne, G.M., 2000a. Taphonomic Control on Microstructure in Early Neoproterozoic Reefal Stromatolites and Thrombolites. Palaios 15 (2), 87–111.
Turner, E.C., James, N.P., Narbonne, G.M., 1997. Growth dynamics of Neoproterozoic calcimicrobial reefs, Mackenzie Mountains, northwest Canada. J. Sediment. Res. 67.
Turner, E.C., Long, D.G.F., 2008. Basin architecture and syndepositional fault activity during deposition of the Neoproterozoic Mackenzie Mountains supergroup, Northwest Territories, Canada. Northwest Territories Geoscience Office Contribution 0040. Can. J. Earth Sci. 45 (10), 1159–1184.
Turner, E.C., Long, D.G.F., 2012. Formal definition of the Neoproterozoic Mackenzie Mountains Supergroup (NWT), and formal stratigraphic nomenclature for its carbonate and evaporate formations. Open File 7112, 57.
Turner, E.C., Narbonne, G.M., James, N.P., 1993. Neoproterozoic reef microstructures from the Little Dal Group, northwestern Canada. Geology 21 (3), 259. https://doi.org/10.1130/0091-7613(1993)021<0259:NRMFTL>2.3.CO;2.
Turner, E.C., Narbonne, G.M., James, N.P., 2000b. Framework composition of early Neoproterozoic calcimicrobial reefs and associated microbialites, Mackenzie Mountains, N.W.T., Canada. In: Grotzinger, J.P., James, N.P. (Eds.), Carbonate Sedimentation and Diagenesis in the Evolving Precambrian World. SEPM Special Publication no. 67, pp. 179–205.
van Acken, D., Thomson, D., Rainbird, R.H., Creaser, R.A., 2013. Constraining the depositional history of the Neoproterozoic Shaler Supergroup, Amundsen Basin, NW Canada: Rhenium-osmium dating of black shales from the Wynniatt and Boot Inlet Formations. Precambr. Res. 236, 124–131.
Veevers, J.J., 2004. Gondwanaland from 650–500 Ma assembly through 320 Ma merger in Pangea to 185–100 Ma breakup: supercontinental tectonics via stratigraphy and radiometric dating. Earth Sci. Rev. 68 (1-2), 1–132.
Voegelin, A.R., Nägler, T.F., Beukes, N.J., Lacassie, J.P., 2010. Molybdenum isotopes in late Archean carbonate rocks: Implications for early Earth oxygenation. Precambr. Res. 182 (1-2), 70–82.
Voegelin, A.R., Nägler, T.F., Samankassou, E., Villa, I.M., 2009. Molybdenum isotopic composition of modern and Carboniferous carbonates. Chem. Geol. 265 (3-4), 488–498.
Voegelin, A.R., Pettke, T., Greber, N.D., von Niederhäusern, B., Nägler, T.F., 2014. Magma differentiation fractionates Mo isotope ratios: evidence from the Kos Plateau Tuff (Aegean Arc). Lithos 190-191, 440–448.
Ward, J.F., Verdel, C., Campbell, M.J., Leonard, N., Duc Nguyen, A.i., 2019. Rare earth element geochemistry of Australian Neoproterozoic carbonate: Constraints on the Neoproterozoic oxygenation events. Precambr. Res. 335, 105471. https://doi.org/10.1016/j.precamres.2019.105471.
Warke, M.R., Di Rocco, T., Zerkle, A.L., Lepland, A., Prave, A.R., Martin, A.P., Ueno, Y., Condon, D.J., Claire, M.W., 2020. The great oxidation event preceded a paleoproterozoic "snowball Earth". Proc. Natl. Acad. Sci. 117 (24), 13314–13320.
Webb, G.E., Kamber, B.S., 2000. Rare earth elements in Holocene reefal microbialites: a new shallow seawater proxy. Geochim. Cosmochim. Acta 64 (9), 1557–1565.
Webb, G.E., Kamber, B.S., 2011. Trace Element Geochemistry as a Tool for Interpreting Microbialites. In: Golding, S.D., Glikson, M. (Eds.), Earliest Life on Earth: Habitats, Environments and Methods of Detection. Springer, Netherlands, Dordrecht, pp. 127–170.
Wei, W., Frei, R., Klaebe, R., Tang, D., Wei, G.Y., Li, D., Tian, L.L., Huang, F., Ling, H.F., 2021. A transient swing to higher oxygen levels in the atmosphere and oceans at~ 1.4 Ga. Precambr. Res. 354, 106058.
Wen, H., Carignan, J., Zhang, Y., Fan, H., Cloquet, C., Liu, S., 2011. Molybdenum isotopic records across the Precambrian-Cambrian boundary. Geology 39 (8), 775–778.
Willbold, M., Elliott, T., 2017. Molybdenum isotope variations in magmatic rocks. Chem. Geol. 449, 253–268.
Willbold, M., Hibbert, K., Lai, Y.-J., Freymuth, H., Hin, R.C., Coath, C., Vils, F., Elliott, T., 2016. High-Precision Mass-Dependent Molybdenum Isotope Variations in Magmatic Rocks Determined by Double-Spike MC-ICP-MS. Geostand. Geoanal. Res. 40, 389–403.
Wille, M., Kramers, J.D., Nägler, T.F., Beukes, N.J., Schröder, S., Meisel, T.h., Lacassie, J. P., Voegelin, A.R., 2007. Evidence for a gradual rise of oxygen between 2.6 and 2.5 Ga from Mo isotopes and Re-PGE signatures in shales. Geochim. Cosmochim. Acta 71 (10), 2417–2435.
Wille, M., Nägler, T.F., Lehmann, B., Schröder, S., Kramers, J.D., 2008. Hydrogen sulfide release to surface waters at the Precambrian/Cambrian boundary. Nature 453, 767–769.
Xu, L., Lehmann, B., Mao, J., Nägler, T.F., Neubert, N., Böttcher, M.E., Escher, P., 2012. Mo isotope and trace element patterns of Lower Cambrian black shales in South China: Multi-proxy constraints on the paleoenvironment. Chem. Geol. 318 (319), 45–59.
Ye, Y., Zhang, S., Wang, H., Wang, X., Tan, C., Li, M., Wu, C., Canfield, D.E., 2021. Black shale Mo isotope record reveals dynamic ocean redox during the Mesoproterozoic Era. Geochem. Perspect. Lett. 18, 16–21.
Zhang, S., Wang, X., Wang, H., Bjerrum, C.J., Hammarlund, E.U., Costa, M.M., Connelly, J.N., Zhang, B., Su, J., Canfield, D.E., 2016. Sufficient oxygen for animal respiration 1,400 million years ago. Proc. Natl. Acad. Sci. 113 (7), 1731–1736.
Zhang, K., Zhu, X., Wood, R.A., Shi, Y., Gao, Z., Poulton, S.W., 2018. Oxygenation of the Mesoproterozoic ocean and the evolution of complex eukaryotes. Nat. Geosci. 11 (5), 345–350.
Zhao, P.P., Li, J., Zhang, L., Wang, Z.B., Kong, D.X., Ma, J.L., Wei, G.J., Xu, J.F., 2016. Molybdenum mass fractions and isotope compositions of international geological reference materials. Geostand. Geoanal. Res. 40 (2), 217–226.